Physica D 240 (2011) 1164–1180

Contents lists available at ScienceDirect

Physica D

journal homepage: www.elsevier.com/locate/physd

Voltage interval mappings for activity transitions in neuron models for elliptic bursters

Jeremy Wojcik, Andrey Shilnikov *

Neuroscience Institute, and Department of Mathematics and Statistics, Georgia State University, 100 Piedmont Ave SE, Atlanta, GA 30303, USA

ARTICLE INFO

Article history:
Received 9 June 2010
Received in revised form
31 March 2011
Accepted 6 April 2011
Available online 20 April 2011
Communicated by V. Rom-Kedar

Keywords:
Poincaré mapping
Elliptic
Bursting
Neuron model
Bifurcation
Periodic orbit

ABSTRACT

We performed a thorough bifurcation analysis of a mathematical elliptic bursting model, using a computer-assisted reduction to equationless, one-dimensional Poincaré mappings for a voltage interval. Using the interval mappings, we were able to examine in detail the bifurcations that underlie the complex activity transitions between: tonic spiking and bursting, bursting and mixed-mode oscillations, and finally mixed-mode oscillations and quiescence in the FitzHugh–Nagumo–Rinzel model. We illustrate the wealth of information, qualitative and quantitative, that was derived from the Poincaré mappings, for the neuronal models and for similar (electro)chemical systems.

1. Pointwise Poincaré mappings and elliptic bursting models

Activity types of isolated neurons and their models may be generically classified as hyper- and depolarizing quiescence, sub-threshold and mixed mode oscillations, endogenous tonic spiking and bursting. Bursting is an example of composite, recurrent dynamics comprised of alternating periods of tonic spiking oscillations and quiescence. The type of bursting in which tonic spiking oscillations alternate with sub-threshold oscillations is often referred to as Mixed Mode Oscillations (MMO). Various endogenous bursting patterns are the natural behavior rhythms generated by central pattern generators (CPG) [1]. A CPG is a neural network, or a mini circuit, controlling various vital repetitive locomotive functions of animals and humans [2]. We contend that understanding all plausible transitions of the activity patterns of individual neuron models would allow for better understanding of networked models. In this study we elaborate on the transition mechanisms by revealing the underlying bifurcations between neuronal activities on the elliptic bursting models of (inter) neurons which are used as the building blocks in the CPG circuitry.

Bursting represents direct evidence of multiple time scale dynamics of a neuron. Deterministic modeling of bursting neurons was originally proposed and done within a framework of three-dimensional, slow–fast dynamical systems. Geometric configurations of models of bursting neurons were pioneered by Rinzel [3,4] and enhanced in [5–8]. The proposed configurations are all based on the geometrically comprehensive dissection approach, or the time scale separation which have become the primary tools in mathematical neuroscience. The topology of the slow motion manifolds is essential to the geometric understanding of neurodynamics. Through the use of geometric methods of the slow–fast dissection, where the slowest variable of the model is treated as a control parameter, it is possible to detect and follow the manifolds made of branches of equilibria and limit cycles in the fast subsystem. Dynamics of a slow–fast system are determined by, and centered around, the attracting sections of the slow motion manifolds [9–16].

The slow–fast dissection approach works exceptionally well for a multiple time scale model, provided the model is far from a bifurcation in the singular limit. On the other hand, a bifurcation describing a transition between neuron activities may occur from reciprocal interactions involving the slow and fast dynamics of the model. Such slow–fast interactions may lead to the emergence of distinct dynamical phenomena and bifurcations that can occur only in the full model, not in either subsystem of the model. As such, the slow–fast dissection fails at the transition where the solution is no longer constrained to stay near the slow motion manifold, or when the time scale of the dynamics of the fast subsystem slows to that of the slow system, near the homoclinic and saddle node bifurcations, for example.

* Corresponding author.
E-mail address: ashilnikov@gsu.edu (A. Shilnikov).

0167-2789/$ – see front matter © 2011 Elsevier B.V. All rights reserved.
doi:10.1016/j.physd.2011.04.003

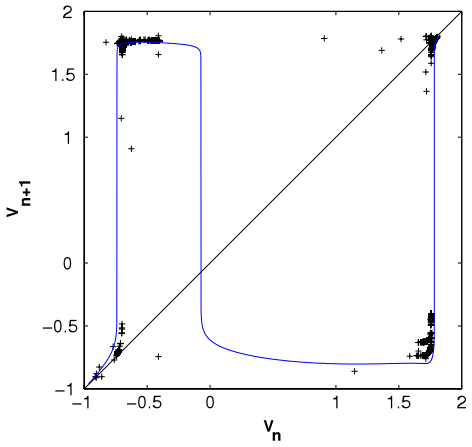

Fig. 1. A point-wise mapping (black +) for the local v-maxima of the bursting solutions starting from randomized initial conditions in the phase space of the FitzHugh–Nagumo–Rinzel model at $c = -0.7$ and overlaid with the "continuous" mapping graph obtained using the proposed technique.

Activity transitions can pose a challenge as the dynamics of a model may become complex and in many instances exhibit deterministic chaos [17–24]. The spectrum of bifurcations and dynamical phenomena that initiate bursting in the models of mathematical neuroscience is rich and includes, but is not limited to, period-doubling cascades, the blue sky catastrophe, multistability, and the formation and subsequent breakdown of a canard-torus in elliptic bursters. Transformative bifurcations of repetitive oscillations, such as bursting, are most adequately described by Poincaré mappings [25], which allow for global bifurcation analysis. Time series based Poincaré mappings have been heavily employed for examinations of voltage oscillatory activities in mathematical neuroscience, as well as other applied sciences [26–29], despite their limitation due to sparseness. Often feasible reductions to mappings of the slowest variable can be achieved through the aforementioned dissection tool in the singular limit [30–34,25]. However, this method often fails for elliptic bursters since no single valued mapping for the slow variable can be derived for the particular slow motion manifold.

Elliptic bursters have been a focus of extensive studies, including deterministic and stochastic modeling, see recently [35–39] and references therein. Elliptic bursting models are not restricted to the realm of neuroscience, however. A feature of elliptic bursters is the occurrence of canard-based MMO [26–28] shown in Insets B of Fig. 3. MMOs are typical for excitable systems describing various (electro)chemical reactions, including the famous Belousov–Zhabotinky reaction [29,40]. One way of examining the core of MMO complex dynamics in such systems experimentally and numerically is to reduce the model to the dynamics of a single, significant variable, such as voltage in neuroscience. Fig. 1 demonstrates the pointwise mapping (black +) generated by the local maxima of the voltage time series initiated from random initial conditions in the phase space of the FitzHugh–Nagumo–Rinzel model, overlaid with a "continuous" mapping (blue) for contrast. The approach, solely available in experimental studies, may typically reveal some selected fragments of the return mappings, very similar to the mappings identified in the (electro)chemical reactions [27,40,28], but not the mapping graph as a whole.

MMOs happen to be a typical phenomenon found in neurophysiology and have been found in elliptic bursters, and are tied to the emergence of the Hopf-initiated canards [41–45] and the references therein. The properties of MMOs, or broadly the current description of transitions between bursting, tonic spiking and subthreshold oscillations in elliptic bursters is incomplete and presents a challenging problem for mathematical neuroscience and the dynamical systems theory in general.

In this paper we refine and expound on the technique of creating a family of one-dimensional mappings, proposed in [18,46,47] for the leech heart interneuron, into the class of elliptic models of endogenously bursting neurons. We will show a plethora of information, both qualitative and quantitative, that can be derived from the mappings to thoroughly describe the bifurcations as such a model undergoes transformations. We also demonstrate the power of deriving not only individual mappings, but the additional benefits of having the entire family of mappings created from an elliptic bursting model. We will also discuss the limitations of our method and show the similarity of our mappings to higher dimensional and biologically plausible models of the elliptic bursters, namely: a bursting adaption of the classical Hodgkin–Huxley model and a realistic Rubin–Terman model for the external segment of the Globus Pallidus.

2. FitzHugh–Nagumo–Rinzel model

The mathematical FitzHugh–Nagumo–Rinzel model of the elliptic burster is given by the following system of equations with a single cubic nonlinear term:

$$\begin{aligned} v' &= v - v^3/3 - w + y + I, \\ w' &= \delta(0.7 + v - 0.8w), \\ y' &= \mu(c - y - v); \end{aligned} \tag{1}$$

here we fix $\delta = 0.08$, $I = 0.3125$ an applied external current, and $\mu = 0.002$ is a small parameter determining the pace of the slow y variable. The slow variable, y, becomes frozen in the singular limit, $\mu = 0$. We employ c as the primary bifurcation parameter of the model, variations of which elevate/lower the slow nullcline given by $y' = 0$. The last equation is held geometrically in a plane given by $v = y - c$ in the three-dimensional phase space of the model, see Fig. 3. The two fast equations in (1) describe a relaxation oscillator in a plane, provided δ is small. The fast subsystem exhibits either tonic spiking oscillations or quiescence for different values of y corresponding to a stable limit cycle and a stable equilibrium state, respectively. The periodic oscillations in the fast subsystem are caused by a hysteresis induced by the cubic nonlinearity in the first "voltage" equation of the model.

Stability loss of the equilibrium state in the fast subsystem is known to be caused by a sub-critical Andronov–Hopf bifurcation which occurs when an unstable limit cycle collapses onto the equilibrium state. Both stable and unstable limit cycles emerge in the fast subsystem through a saddle–node bifurcation. Using a traditional slow–fast dissection, one can locate and continue the corresponding branches, labeled by $M_{\rm lc}$ and $M_{\rm eq}$ in Fig. 3, composed of the limit cycles and equilibrium states respectively, of the fast subsystem by varying the frozen y variable in the extended $(v, w; y)$-phase space of the model (1).

Fig. 3(A) presents a 3D view of the slow motion manifolds in the phase space of the FitzHugh–Nagumo–Rinzel model. The tonic spiking manifold $M_{\rm lc}$ is composed of the limit cycles for the model (1), both stable (outer) and unstable (inner) sections. The fold on $M_{\rm lc}$ corresponds to a saddle–node bifurcation, where the stable and unstable branches merge. The vertex, where the unstable branch of $M_{\rm lc}$ collapses at $M_{\rm eq}$, corresponds to a subcritical Andronov–Hopf bifurcation. The manifold $M_{\rm eq}$ is the space curve made from equilibria of the model. The intersection of the plane, $y' = 0$ with the manifold, determines the location of the existing equilibrium state for a given value of the bifurcation parameter c: stable (saddle-focus) if located before (after) the Andronov–Hopf bifurcation point on the solid (dashed) segment of $M_{\rm eq}$. The plane, $y' = 0$, is called the slow nullcline, above (below) which the y component of a solution of the model increases (decreases). The plane moves in the 3D phase space as

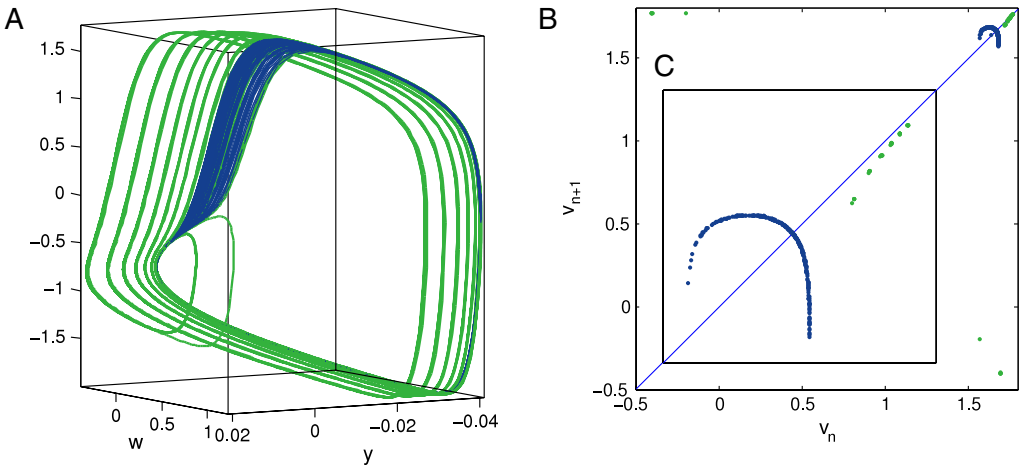

Fig. 2. (A) Transient solution in the FitzHugh–Nagumo–Rinzel model for $c = -0.6192979$ on the transition from chaotic tonic spiking (blue) to bursting (green), and (B) the corresponding pointwise return mapping for the local v-maxima. Inset (C) gives the magnification of the mapping section revealing the period-doubling cascade preceding the transition from tonic spiking to bursting (for comparison with the mappings in Figs. 13 and 14 obtained using the technique proposed in this paper). (For interpretation of the references to colour in this figure legend, the reader is referred to the web version of this article.)

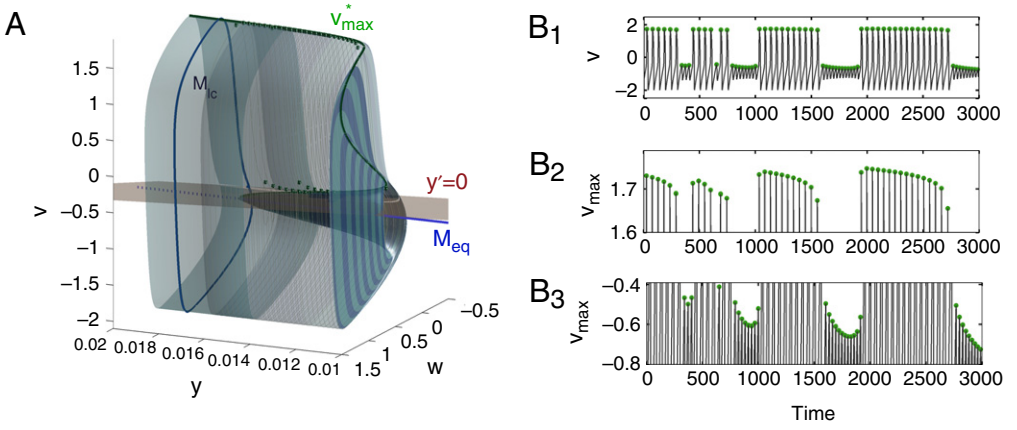

Fig. 3. (A) Topology of the tonic spiking, M_{lc}, and quiescent, M_{eq} manifolds. Solid and dashed branches of M_{eq} are made of stable and unstable equilibria of the model, resp. The space curve, labeled by V^*_{max} (in green) corresponding to the v-maximal coordinates of the periodic orbits composing M_{lc}. An intersection point of $y' = 0$ with M_{eq} is an equilibrium state of (1). Shown in grey is the bursting trajectory traced by the phase point: the number of spikes per burst is the same as the number of turns the phase point makes around M_{lc}. Spikes are interrupted by the periods of quiescence when the phase point follows M_{eq} after it falls from M_{lc} near the fold. (B_1) A voltage trace for $c = -0.67$, displaying the voltage evolution in time as the phase point travels around the slow motion manifolds. Green dots at the voltage maxima correspond to the green spheres on V^*_{max} in (A). (B_2) While the maximal voltages in inset (B_1) appear to be constant, enlarging the maxima reveals significant variations in the v-maximal values. (B_3) Enlargement for the subthreshold voltage oscillations. (For interpretation of the references to colour in this figure legend, the reader is referred to the web version of this article.)

the control parameter c is varied. When the slow nullcline cuts through the solid segment of M_{eq}, the model enters a quiescent phase corresponding to a stable equilibrium state. Raising the plane to intersect the unstable (inner) cone-shaped portion of M_{lc} makes the equilibrium state unstable through the Andronov–Hopf bifurcation, which is subcritical in the singular limit, but becomes supercritical at a given value of the small parameter $\varepsilon = 0.002$, see Fig. 6(A). Continuing to raise the slow nullcline by increasing c gives rise to bursting represented by solutions following and repeatedly switching between M_{eq} and M_{lc}. Bursting occurs in the model (1) whenever the quiescent M_{eq} and spiking M_{lc} manifolds contain no attractors, i.e. neither a stable equilibrium state nor a stable periodic orbit exist. The number of complete revolutions, or "windings", of the phase point around M_{lc} corresponds to the number of spikes per burst. The larger the number of revolutions the longer the active phase of the neuron lasts. Spike trains are interrupted by periods of quiescence while the phase point follows the branch M_{eq}, onto which the phase point falls from M_{lc} near the fold, see Fig. 3. The length of the quiescent period, as well as the delay of the stability loss (determined mainly, but not entirely, by the small parameter μ), begins after the phase point passes through the subcritical Andronov–Hopf bifurcation onto the unstable section of M_{eq}. Further increase of the bifurcation parameter, c, moves the slow nullcline up so that it cuts through the stable cylinder-shaped section of the manifold M_{lc} far from the fold. This gives rise to a stable periodic orbit corresponding to tonic spiking oscillations in the model.

In this paper we are most interested in the scenarios or the sequence of bifurcations which the solutions of the model undergoes near the transitions between tonic spiking, bursting and quiescence. MMOs occur at the transition between bursting and quiescence. Prior to the onset of MMO, the model demonstrates a plethora of small amplitude, subthreshold oscillations due to the emergence and breakdown of an invariant torus, followed by a period-doubling cascade involving unstable periodic orbits, see Figs. 5(B) and 19.

The transition from tonic spiking and bursting is accompanied by another sequence of period-doubling bifurcations. The bifurcation starts when the stable periodic orbit reaches the fold of M_{lc} and becomes unstable, Fig. 5(A), depicting the first three stages of the

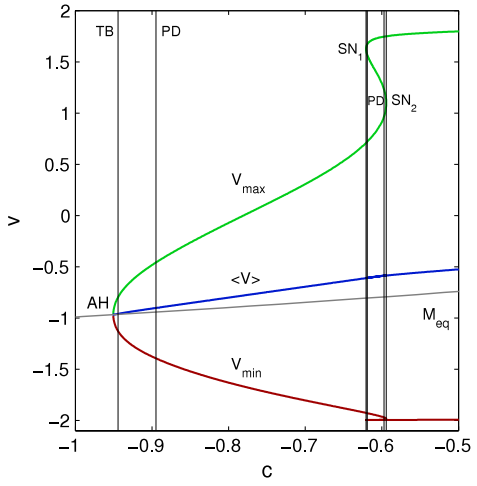

Fig. 4. (V, c)-bifurcation diagram for the full model showing the intervals of tonic spiking, bursting and quiescence in the model. All three branches of maximal $V_{\max}$, averaged $\langle V\rangle$, and minimal $V_{\min}$ values of the voltage variable of the periodic orbits emerge from the subcritical Andronov–Hopf bifurcation (AH). Note two folds corresponding to two saddle–node bifurcations occurring en route from bursting to tonic spiking. Fig. 1 gives the corresponding 3D view of the tonic-spiking and quiescent manifolds found parametrically, i.e. as the parameter c is varied, in the phase space of the FitzHugh–Nagumo–Rinzel model.

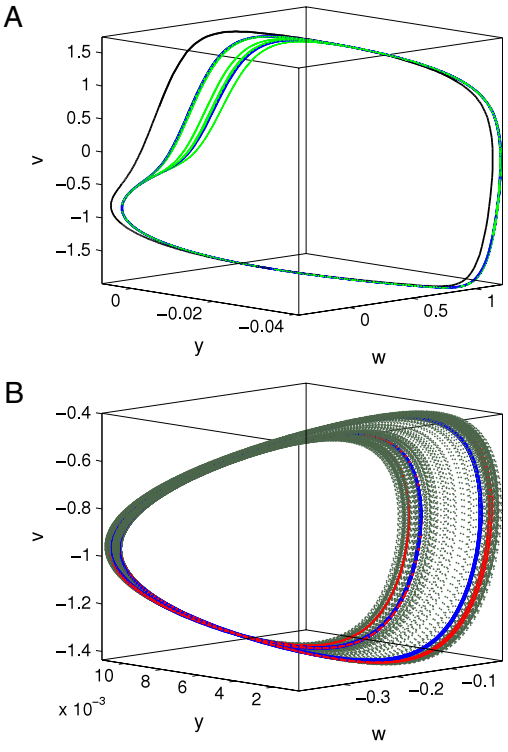

Fig. 5. (A) Period-doubling cascades showing the large tonic spiking orbits of period-1 at $c = -0.6$, period-2 at -0.6192 and of period-16 at -0.61926. (B) Unstable subthreshold oscillations of period-1 at $c = 0.894$, period-4 at -0.89335 and chaotic at -0.89307.

cascade. Geometrically, this transition takes place while the slow nullcline is lowered through the fold at $\varepsilon = 0.002$ on the space curve $\langle v\rangle$ for the averaged values of the v coordinate of the periodic orbits composing the slow-motion manifold, $M_{\rm lc}$. The bifurcation diagram in Fig. 4 elucidates there are at least two saddle–node bifurcations involved in addition to the period-doubling cascade. This is confirmed by the fragmentary pointwise mapping in Fig. 2 taken at the transition between tonic spiking and bursting.

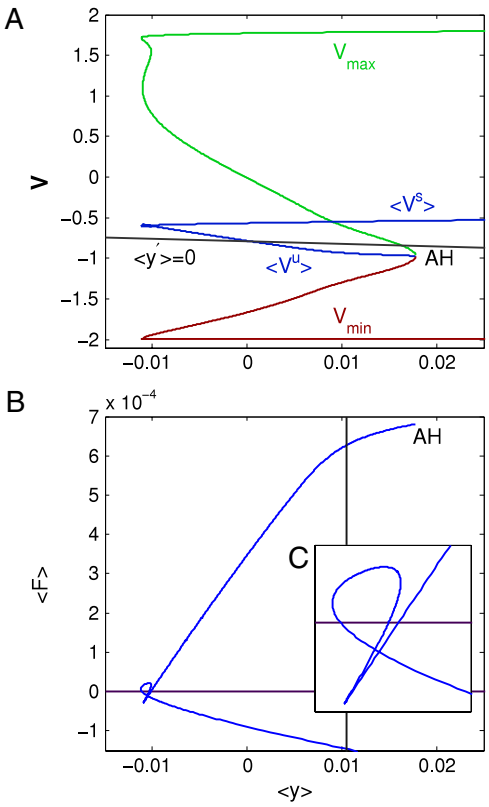

Fig. 6. (A) Maximal $V_{\max}$, averaged $\langle V\rangle$, and minimal $V_{\min}$ branches plotted against the averaged $\langle y\rangle$ variable of the periodic orbits moving along the tonic spiking manifold $M_{\rm lc}$ as the bifurcation parameter c is varied. The slow nullcline $\langle y'\rangle = 0$ at $c = -0.79$ passes through the unstable segment of $\langle V\rangle$ between the AH point and the fold for bursting to occur in the model. (B) A zero, around 0.00105, of the averaged function $\langle F\rangle$ defined in (2) plotted against $\langle y\rangle$ corresponds to a hyperbolic equilibrium states of the average equation, and respectively to a stable periodic orbit on $M_{\rm lc}$. Inset (C) shows a zoomed-in section of the graph of $\langle F\rangle$ near the fold in question, where the latter becomes a multi-valued function indicating the failure of the averaging approach near the transition at $c = -0.61$.

2.1. Averaging method: pros and cons

The averaging method, introduced for slow–fast systems by Pontryagin and Rodygin [13], may also be utilized. The averaging method employs the detection of bifurcations for periodic orbits by reducing the problem to stability analysis of corresponding equilibrium states to a single average equation for the slow variable, y in the model (1). The average equation is obtained by making a parameter sweep for periodic orbits along the two-dimensional manifold $M_{\rm lc}$ in the phase space of the entire model. Suppose that the model, at $\mu = 0$, has a $T(y)$-periodic orbit given by $v = \varphi(y, v_0)$. Due to continuity the evolution of the y coordinate of the phase point for $|\mu| \ll 1$ near the normally hyperbolic (i.e. far from bifurcations) portion of $M_{\rm lc}$ can be evaluated in first order approximation by the following average equation:

$$\langle y'(t)\rangle = \frac{\mu}{T(y)}\int_0^{T(y)} (c - y - \varphi(y, v_0))\,dt$$
$$\simeq \mu(c - \langle y\rangle - \langle v(y)\rangle) \triangleq \langle F(y, c)\rangle, \qquad (2)$$

where $\langle v(y)\rangle$ is the v coordinate of the periodic orbit averaged over the period. Note that Eq. (2) preserves the linear relation of the arguments. The graph of the function $\langle F\rangle$ in the right-hand side of (2) is shown in Fig. 6(B). A simple zero of $\langle F(y, c)\rangle$ is an equilibrium state, stable or not, of the average equation that corresponds to a periodic orbit on $M_{\rm lc}$ of the whole model. This periodic orbit could be stable, repelling (totally unstable),

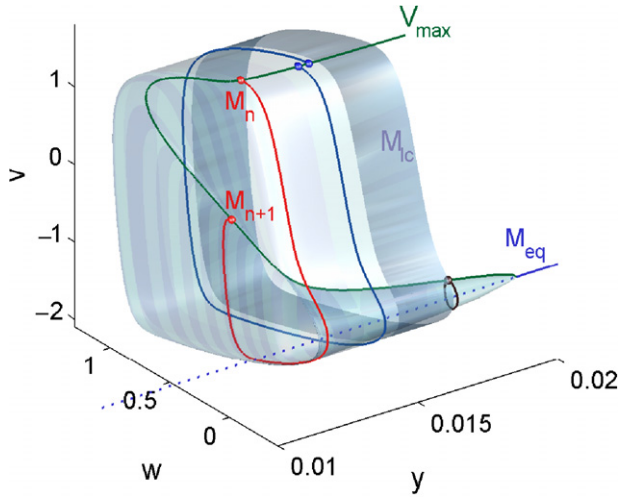

Fig. 7. Three sample orbits demonstrating the construction of the return mapping $T: M_n \to M_{n+1}$ defined for the points of the cross-section $V_{\max}$ on the manifold $M_{\rm lc}$. Singling out the v coordinates of the points gives pairs (V_n, V_{n+1}) constituting the voltage interval mapping at a given parameter, c.

or of the saddle type. The stability depends on: (1) location on the stable/unstable, in the (v, w)-plane, section of $M_{\rm lc}$ and (2) whether the graph of $\langle F(y, c)\rangle$ increases or decreases at the given zero. Variations of the bifurcation parameter c translate the graph of $\langle F\rangle$ vertically. The graph of the bi-folded average function in the right-hand side of (2) is interpreted as follows: the low section of the graph corresponds to $\langle F\rangle$ evaluated on the stable, cylinder-shaped portion of $M_{\rm lc}$, whereas the upper section corresponds to $\langle F\rangle$ evaluated on the repelling, cone-shaped portion which terminates at the Andronov–Hopf bifurcation. The averaging technique elucidates whether there exists a periodic orbit on either section of $M_{\rm lc}$. The interpretation of the average equation is ambiguous near the fold, when $c = -0.61$.

The bi-valued graph of $\langle F\rangle$ showing the separation into the sections of $M_{\rm lc}$ is no longer obvious: the magnification of $\langle F\rangle$ in Fig. 6(C) indicates that there should be two saddle–node bifurcations corresponding to double zeros of $\langle F\rangle$. One zero is from a sharp cusp, whereas the other saddle–node, for a smaller value of c, would yield a proper quadratic tangency typical for such a bifurcation (this assertion is supported by examination of the mappings in Fig. 7). Inset (C) of Fig. 6 shows that the bifurcation sequence at this transition is more complex then a trivial stability loss or disappearance of the round tonic spiking orbit at the fold. Consequently, we need tools more advanced than the slow–fast dissection or average differential equation (2) for the global examination of the dynamics of the model. Examination of the global dynamics can be accomplished through a reduction to the interval Poincaré return mappings, which allow for an accurate description of complex oscillatory behaviors and bifurcations, such as period doubling, for solutions of the model.

3. Voltage interval mappings

Methods of the global bifurcation theory are organically suited for examinations of recurrent dynamics such as tonic spiking, bursting and subthreshold oscillations [41,48,49], as well as their transformations. The core of the method is a reduction to and derivation of a low dimensional Poincaré return mapping with an accompanying analysis of the limit solutions; fixed, periodic and homoclinic orbits each representing various oscillations in the original model. Mappings have been actively employed in computational neuroscience, see [50,30,31,44,45] and references therein. It is customary that such a mapping is sampled from voltage traces, for example by identifying successive voltage maxima, minima, or interspike intervals [51], Fig. 3(B_1). Notice that the v-maxima in the voltage trace, Fig. 3(B_1), appear constant. However, the enlargements in Insets (B_2) and (B_3) show considerable variation in the v-maxima of the voltage traces. A drawback of a mapping generated by time series is sparseness, see Fig. 1, as the construction algorithm reveals only a single periodic attractor of a model, unless the latter demonstrates chaotic or mixing dynamics producing a large variety of densely wandering points. Chaos may also be evoked by small noise whenever the dynamics of the model are sensitively vulnerable to small perturbations that do not substantially re-shape intrinsic properties of the autonomous model [47,39]. Small noise, however, can make the solutions of the model wander, thus revealing the mapping graph.

A computer-assisted method for constructing a complete family of Poincaré mappings for an interval of membrane potentials for slow–fast Hodgkin–Huxley models of neurons was proposed in [46] following [52]. Having a family of such mappings we are able to elaborate on various bifurcations of periodic orbits, examine bistability of coexisting tonic spiking and bursting, and detect the separating unstable sets that are the organizing centers of complex dynamics in any model. In this paper we employ and enhance this technique to understand the bifurcations underlying the transitions between various activity types in the models of the elliptic bursters. Examination of the mappings will help us make qualitative predictions about transitions *before* the transitions occur in models.

By construction, the mapping T takes the space curve $V^*_{\max}$ into itself after a single revolution around the manifold $M_{\rm lc}$, Fig. 7, i.e. $T : V_n \to V_{n+1}$. This technique allows for the creation of a Poincaré return mapping; taking an interval of the voltage values into itself. The found set of matching pairs (V_n, V_{n+1}) constitutes the graph of the Poincaré mapping for a selected parameter value c. Provided the number of paired coordinates is sufficiently large and applying a standard spline interpolation we are able to iterate trajectories of the mapping, compute Lyapunov exponents, evaluate the Schwarzian derivative, extract kneading invariants for the topological entropy, and many other quantities.

Varying the parameter, c, we are able to obtain a dense family that covers all behaviors, bifurcations and transitions of the model (1). A family of the mappings for the parameter, c, varied within the range $[-1, -0.55]$ is shown in Fig. 8. Indeed, for the sake of visibility, this figure depicts a sampling of mappings that indicate evolutionary tendencies of the model. A thorough examination of the family allows us to foresee changes in model dynamics. A family of mappings allows us to analyze all the bifurcations whether stable or unstable fixed and periodic orbits including homoclinic and heteroclinic orbits and bifurcations. By following the mapping graph we can predict a value of the parameter at which the corresponding periodic orbit will lose stability or vanish, for example giving rise to bursting from tonic spiking.

A fixed point, $v^\star$, is discerned from the mapping as an intersection of the graph with the bisectrix. Visually we determine the stability of the fixed point by the slope of the graph at the fixed point. If the slope of the graph is less than 1 in absolute value the point is stable. When the slope of the graph at the fixed point is greater than 1 in absolute value the fixed point is unstable. Alternatively stability may be determined from forward iterates of an initial point in the neighborhood of the fixed point which converges to the fixed point. Two generic bifurcations through which a stable fixed point becomes unstable or disappears in a plane are: (1) a flip (period-doubling bifurcation), and (2) fold (saddle–node), respectively. The latter occurs when the mapping graph becomes tangent to a bisectrix. Prior to the fold bifurcation there are two fixed points, stable and unstable, on the bisectrix. After the bifurcation, both fixed points have merged and been

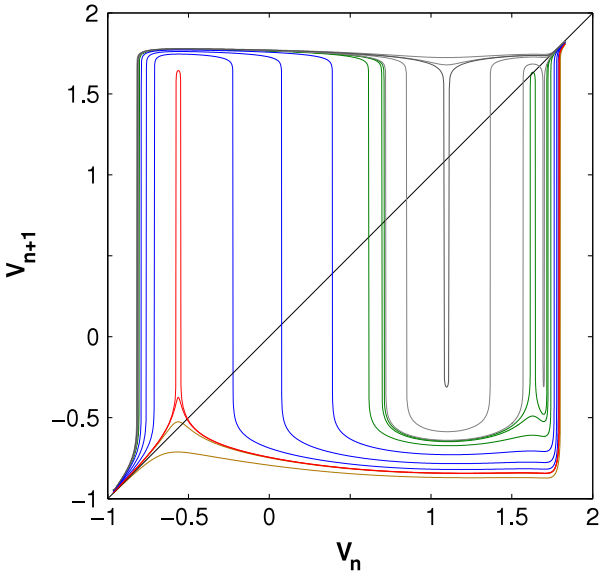

Fig. 8. Coarse sampling of the c-parameter family of the Poincaré return mappings $T : V_n \to V_{n+1}$ for the FitzHugh–Nagumo–Rinzel model at $\mu = 0.002$ as c decreases from $c = -0.55$ to $c = -1$. The grey mappings correspond to the dominating tonic spiking activity in the model. The green mappings show the model transitioning from tonic spiking to bursting. The blue mappings correspond to the bursting behavior in the model. The red mappings show the transition from bursting to quiescence. The orange mappings correspond to the quiescence in the model. An intersection point of a mapping graph with the bisectrix is a fixed point, v^*, of the mapping. The stability of the fixed point is determined by the slope of the mapping graph, i.e. it is stable if $|T'(v^*)| < 1$. Nearly vertical slopes of graph sections are due to an exponentially fast rate of instability of solutions (limit cycles) of the fast subsystem compared to the slow component of the dynamics of the model.

annihilated through the tangency. The flip bifurcation, as a supercritical flip for example, gives rise to the emergence of a period-2 orbit after the fixed point loses stability, where the multiplier becomes less than -1. Flip bifurcations often initiate a period-doubling cascade bifurcation. In our case, such a cascade will be shown to cause chaotic subthreshold oscillations and, once mixed with large amplitude bursting, will give rise to MMO.

3.1. Materials and methods

Paramount to the process of creating the voltage interval return mapping is the generation of the slow motion manifolds for the model. We have developed a practical approach for the localization of manifolds in the phase space of a slow–fast neuronal model using the parameter continuation technique [53]. The core of the parameter continuation technique is to scan the static manifold in question by translating the slow nullcline in the phase space as the bifurcation parameter is varied. This is possible since a feature of a slow–fast model is that the solutions are constrained to stay near the slow-motion manifolds that are composed of equilibria and periodic orbits of the fast subsystem. Let there be a stable, round periodic orbit of the entire model (1) for some c on the outer section of the tonic spiking manifold M_{lc}. Variations of c moving the slow nullcline in the v-direction make the periodic orbit slide along M_{lc}, thereby revealing the manifold. Hence without slow–fast dissection, but rather by parametrically continuing the periodic orbit, we detect the sought manifold M_{lc}, see Fig. 4. This parameter continuation approach yields the slow manifolds themselves for a given ε. We stress that our approach has been proven to work exceptionally well for several high-dimensional (12D and 14D) models of neurons [46] (including the 5D Terman–Rubin model below), in which application of the standard slow–fast dissection for accurately singling out several subsystems becomes problematic due to the presence of multiple time scales of the state variables.

The slow motion manifold, M_{lc}, is found by following the branch of the periodic orbits of the model starting from a subcritical Andronov–Hopf bifurcation using the parameter continuation software package CONTENT 1.55 [53]. Each of 5840 orbits are sought with a mesh of 401 points. To determine the exact location corresponding to a local maximum $v' = 0$, we use a close point from the mesh data to shoot a solution by integrating the full model in the MATLAB `ode15s` solver with `events` set as follows: absolute tolerance 10^{-11}, relative tolerance 10^{-11}, BDF '`on`'. We repeat this process for each limit cycle of the manifold, hence creating the smooth curve V^*_{max} (green in Fig. 3). We then utilize the set $\{V^*_{\text{max}}\}$ as initial conditions and integrate the model (1) again; stopping integration when the next maxima is reached for each member of $\{V^*_{\text{max}}\}$. Thus we created a new set of pairs (V_n, V_{n+1}), where $V_n \in \{V^*_{\text{max}}\}$ and V_{n+1} is found from integration of the model (1), see Fig. 7. We then graph the pairs (V_n, V_{n+1}) and used a cubic spline to computationally smooth the data. This allows us to compute trajectories of the mappings. Hence we create *continuous* (computationally smooth) mappings that can be fully analyzed.

4. Qualitative analysis of mappings

The family of mappings, given in Fig. 8, allows for global evolutionary tendencies of the model (1) to be qualitatively analyzed. One can first see the flat mappings in grey have a single fixed point corresponding to the tonic spiking state. We can further deduce the saddle–node bifurcation that gives birth to the two unstable fixed points, at the mapping and bisectrix crossing. The fixed points diverge from each other and one fixed point moves towards the stable fixed point in the upper corner. We can now predict that bursting will be born through another saddle–node bifurcation. The green mappings show the actual transition and saddle–node bifurcation after which we have regular bursting patterns, blue mappings. We also see the other unstable fixed point clearly moving to the lower corner. The red mappings indicate the transition from bursting to quiescence, as the fixed point changes stability.

A major benefit of using the voltage interval mapping is that we are able to understand transitions between the activity states of the model by analyzing and comparing the bifurcations between the states. Activity transitions commonly occur in a slow–fast model near the bifurcations of the fast subsystem where the description of dynamics in the singular limit is no longer accurate because of the failure of (or interpretation of) the slow–fast dissection paradigm. This happens, for example, when the two-dimensional fast subsystem of the model (1) is close to a saddle–node bifurcation (near the fold on the tonic spiking manifold M_{lc}) where the fast dynamics become of the time scale of the slow subsystem. Such an interaction may cause new peculiar phenomena, such as torus formation and subsequent breakdown near the fold on the spiking manifold [54,44]. We return to the torus bifurcation in the Discussion section below. We now turn our attention to a more thorough analysis of the individual mappings.

4.1. Transition from tonic spiking to bursting

Figs. 9–13 elucidate the transformative stages of the voltage mappings for $c \in [-0.594, -0.620625]$ as the dynamics transform from periodic tonic spiking to complex bursting while the FitzHugh–Nagumo–Rinzel model is being "hyperpolarized". It should be stated again that though the given model is a purely phenomenological model with variables and parameters without any biophysical correlation to exact models of neurons, it produces dynamics with vivid similarities typical for the many models within the elliptic bursting class and real neurons.

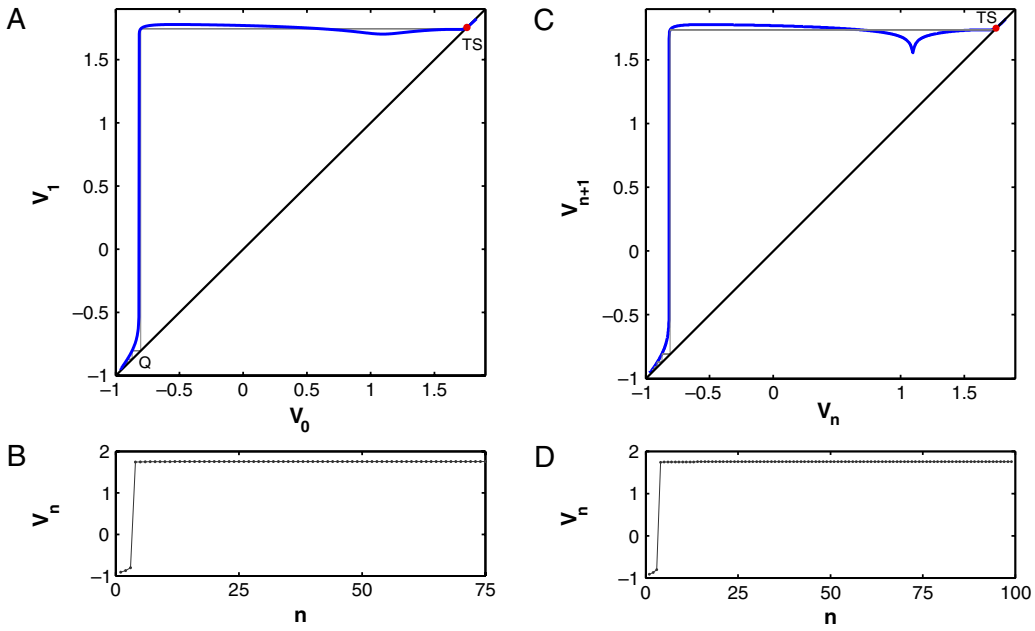

Fig. 9. (A) Poincaré return mapping for the FitzHugh–Nagumo–Rinzel model at $c = -0.59$ has a single stable fixed point, TS, at the upper corner corresponding to a single v-maximum of the tonic spiking periodic orbit on the manifold M_{lc}. Iterates (grey) of an initial point starting near Q show a rapid convergence to the tonic spiking point. (B) Voltage trace shows a rapid establishment of tonic spiking activity. (C) Return mapping at $c = -0.594255$. The convex section from (A) has turned into a cusp and illustrate an imminent saddle node bifurcation. (D) Voltage trace shows that the tonic spiking attractor still dominates the dynamics of the model without any indication of the emergence of the new fixed points.

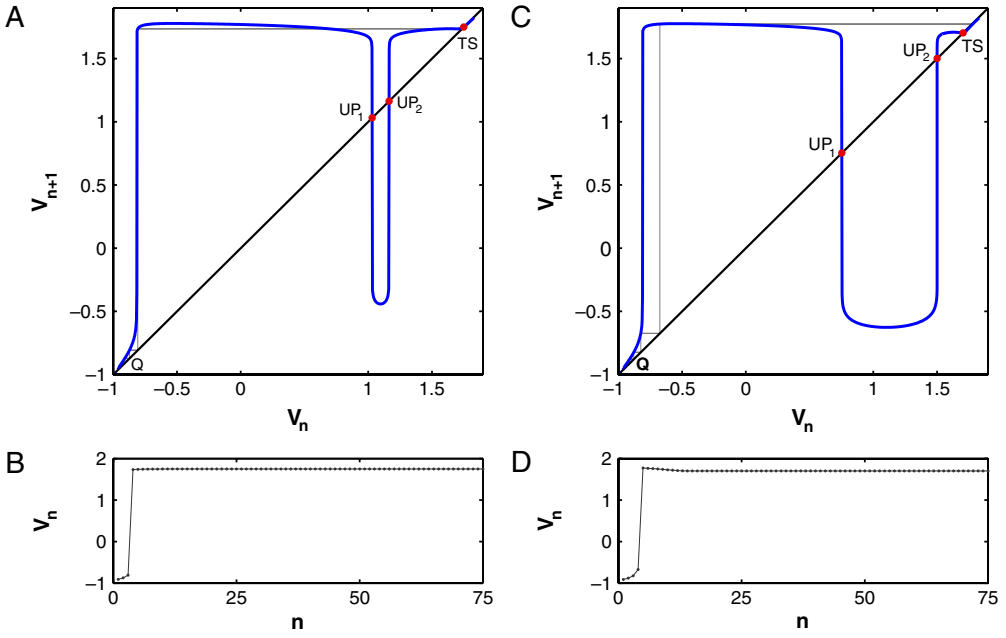

Fig. 10. (A) Poincaré mapping at $c = -0.595$ depicts the formation of 2 unstable fixed points immediately after a saddle node bifurcation. (C) Poincaré mapping at $c = -0.615$ depicts the beginning of a hidden transformation aimed to terminate the tonic spiking stable fixed point TS through the secondary saddle–node bifurcation. (B and D) The corresponding traces of maximal voltage values.

We begin where the model is firmly in the tonic spiking regime at $c = -0.59$. Tonic spiking is caused by the presence of a stable periodic orbit located far from the fold on the manifold M_{lc} (Fig. 3). The only v-maximum of this orbit corresponds to a stable fixed point, labeled TS in Fig. 9(A). The flat section of the mapping graph adjoining the stable fixed point clearly indicates a rapid convergence to the point in the v-direction, as shown by the trace in inset (B). The point, Q, of the mapping located at the quiescent level at $V = -1$ corresponds to the terminal vertex where the tonic spiking manifold, M_{lc}, merges with the quiescent manifold, M_{eq}, through the subcritical Andronov–Hopf bifurcation, Fig. 3. Here the slope of the mapping reflects the exponential instability (stability) of the quiescent (tonic spiking) branch, made of unstable equilibria and stable limit cycles of the fast subsystem of the model.

We next examine the mapping in Fig. 9(C), (D), taken for the parameter $c = -0.594255$. Compared to the upper mapping branches in the family represented in Fig. 8, one can clearly spot a definite trend resulting in a change of the mapping shape where the convex portion has begun turning into a cusp around $V_0 \approx 1.1$, Fig. 9(C), (D). The formation of the cusp is an indication of a

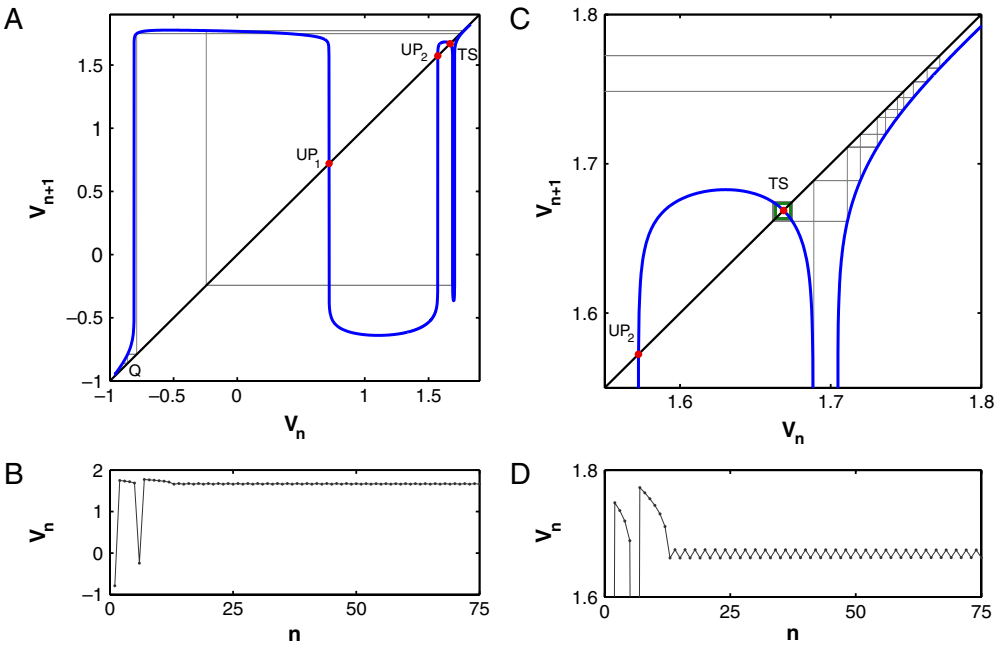

Fig. 11. (A) Poincaré mapping at $c = -0.6193$ and the voltage trace in (B) both demonstrate chaotic bursting transients. (C) Enlargement of the right top corner of the mapping shows that the tonic spiking fixed point has lost stability through a supercritical period-doubling bifurcation. The new-born period-2 orbit is a new attractor of the mapping, as confirmed by the zigzagging voltage trace represented in (D).

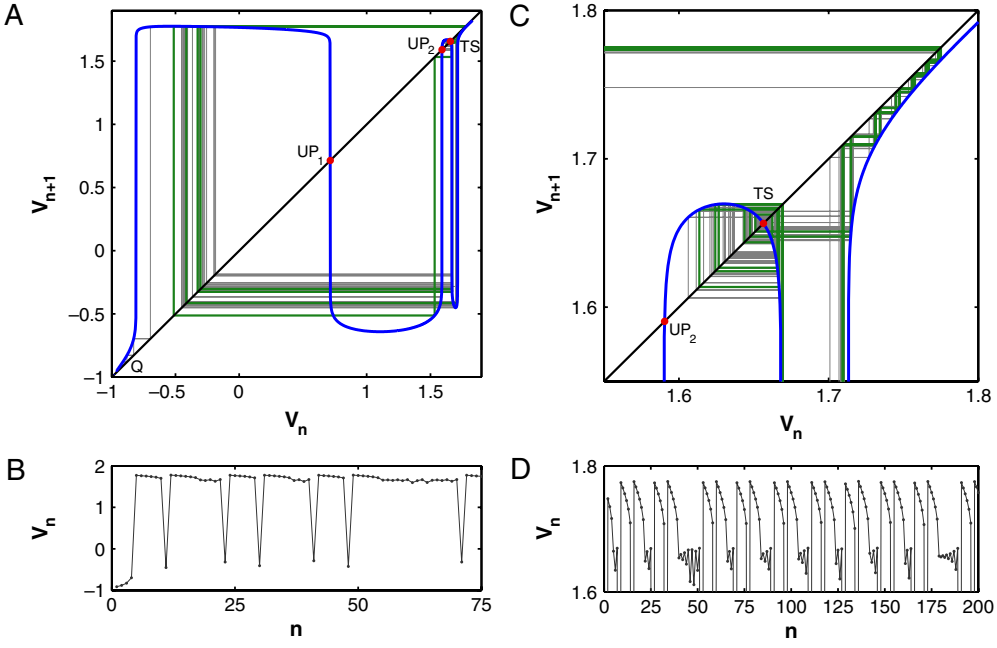

Fig. 12. (A) Chaotic bursting in the mapping at $c = -0.62$. Fixed point TS has become unstable thus initiating a cascade of period-doubling bifurcations, as the local segment of the mapping graph near TS changes concavity. The shape of the mapping elucidates the effects of small perturbations on the model, which could result in iterates at drastically different locations caused by the chaotic behavior. Each spike train is followed by a quiescent period to the left from the threshold UP_1, separating it from the spiking zone (on the right). (B) Chaos is clearly evident in the voltage trace as bursts vary in length (number of spikes) and amplitude. (C) The magnification of the right upper corner of the mapping reveals that chaotic bursting is due to a cascade of period-doubling bifurcations that locally raises the instability level of the mapping. (D) Upper portion of chaotic burst trains.

change in dynamics for the mapping. Thus the mapping insinuates a transition in dynamics of the model (1) prior to it becomes noticeable in the model itself. Note that the maximal voltage trace provides no indication of any eminent transition in the model's behavior.

The mapping in Fig. 10(A) and (B), taken for the parameter $c = -0.595$, clearly illustrates that after the cusp has dropped below the bisectrix, then two additional fixed points, UP_1 and UP_2, are created. UP_1 and UP_2 have emerged through a preceding fold or saddle–node bifurcation taking place at some intermediate parameter value between $c = -0.594255$ and $c = -0.595$. We draw the reader's attention to the (v, c)-bifurcation diagram in Fig. 4. The diagram reveals two turning points labeled SN_1 and SN_2, corresponding to saddle–node bifurcations that occur near the geometric fold on the tonic spiking manifold M_{lc}. The saddle–node bifurcation in the mapping here corresponds to the turning point

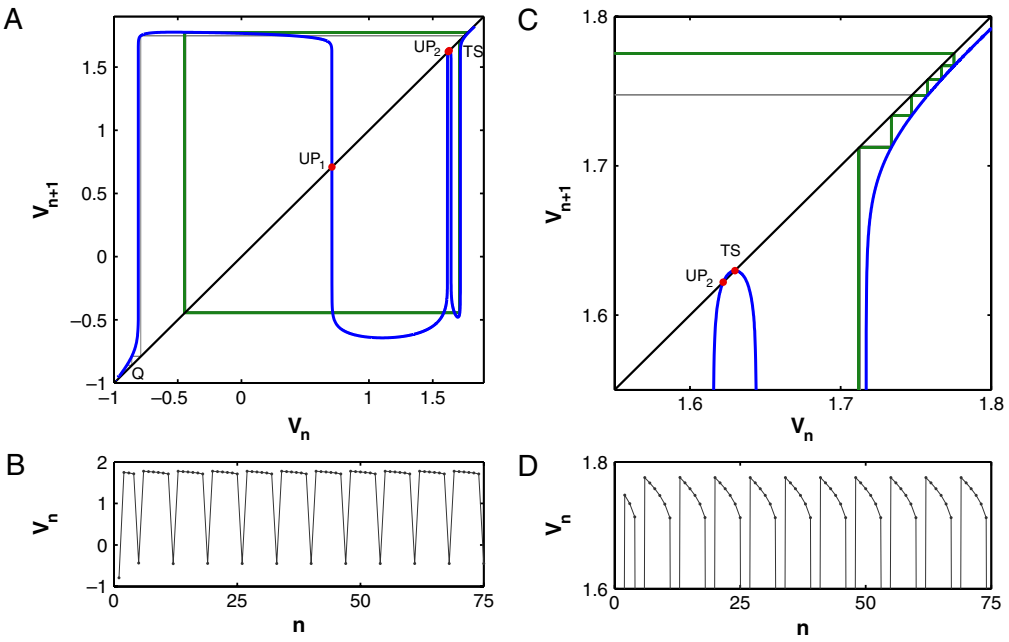

Fig. 13. (A) Return mapping at $c = -0.620625$ demonstrates regular bursting with six spikes per burst followed by a single quiescent point located to the left from the threshold UP_1. This period-6 bursting orbit co-exists with a stable fixed point TS that has a narrow attraction basin. (B) The corresponding bursting trace. (C) The magnification of the right upper corner of the mapping $c = -0.620625$ shows the coexistence of a stable tonic spiking fixed point (TS) and period-6 bursting orbit. Both points, TS and UP_2, are about to annihilate through a saddle–node bifurcation. (D) Voltage trace shows that the magnitude of spikes does decrease to the end of the burst. The number of the spikes per burst equates to the number of iterates the phase point makes near the section of the mapping tangent to the bisectrix.

SN_1 occurring on route from tonic spiking to bursting. Again, let us stress that the singular limit of the model at $\mu = 0$ gives a single saddle–node bifurcation through which the tonic spiking periodic orbit loses stability after it reaches the fold on the tonic spiking manifold. We point out that for an instant the model becomes bistable right after the saddle–node bifurcation in Fig. 9 leading to the emergence of another stable fixed point with an extremely narrow basin of attraction. Here, as before the hyperbolic tonic spiking fixed point, TS, dominates the dynamics of the model.

Fig. 10(C) demonstrates that as the parameter is decreased further to $c = -0.615$, the gap between the new fixed points widens as the point UP_2 moves toward the stable tonic spiking point, TS, to form a fold, SN_1 corresponding to the second saddle–node bifurcation on the route from tonic spiking to bursting documented in the diagram in Fig. 4. Through this saddle–node bifurcation, these fixed points merge and annihilate each other; thereby terminating the tonic spiking activity in the FitzHugh–Nagumo–Rinzel model. Before that happens, several bifurcations involving the fixed point, TS, drastically reshape the dynamics of the model. First, the multiplier becomes negative around $c = -0.619$, that is the first indication of an impending period-doubling cascade. This is confirmed by the mapping at $c = -0.6193$ in Fig. 11(C) and (D) showing that the fixed point has become unstable through the supercritical period-doubling bifurcation. This period-doubling bifurcation gives rise to a stable period-2 tonic spiking orbit in the mapping and to a stable orbit of the doubled period compared to that of the pre-bifurcating tonic spiking orbit in the phase space of the model (1). The location of the period-doubling bifurcation may be identified by simple geometric means in the bifurcation diagram in Fig. 4. Indeed, let us observe that once the fixed point becomes unstable, the multiplier becomes less than -1. Geometrically this implies that the fixed point slides from the concave up to the concave down section of the mapping graph. Therefore the inflection point between the folds in the bifurcation diagram, Fig. 4, corresponds to the given period-doubling bifurcation. Another inflection point, labeled PD, on the unstable branch in the diagram corresponds to a period-doubling bifurcation of a subthreshold periodic orbit discussed below.

The new-born period-2 orbit becomes the new tonic spiking attractor of the mapping. Observe from the voltage trace in Fig. 11(B) and (C) the long transient bursting behavior, thus indicating that boundaries of the attraction basin of the period-2 orbit become fractal. Next, the model approaches bursting onset, chaotic at first as represented in Fig. 12. This figure depicts the behavior of the mapping at $c = -0.62$ and shows the rapid bifurcation sequence that eliminates the period-2 attractor causing the mapping to initiate chaotic dynamics at the transition from tonic spiking to bursting. Correspondingly, the FitzHugh–Nagumo–Rinzel model starts generating chaotic trains of bursts with randomly alternating numbers of spikes per burst. The number of spikes depends on how close the trajectory of the mapping comes to the unstable (spiraling out) fixed point, TS, that is used to represent the tonic spiking activity. Each spike train is interrupted by a single quiescent period. The fixed point UP_1 sets a threshold between the quiescent (left) and tonic spiking (right) sections of the mapping graph. This unstable point corresponds to a saddle periodic orbit of the model, that is located on the unstable, cone-shaped section of the tonic spiking manifold M_{lc} in Fig. 3. Recall that this saddle periodic orbit is repelling in the fast variables and stable in the slow variable.

By comparing Figs. 9–12 one could not foresee that the secondary saddle–node bifurcation eliminating the tonic spiking fixed point TS, or corresponding round stable periodic orbit on the manifold M_{lc}, would be preceded by a dramatic concavity change in the mapping shape causing a forward and inverse cascade of period-doubling bifurcations right before the tonic spiking orbit TS. Observe that regular or periodic bursting emerges before the disappearance of the tonic spiking orbit through the saddle–node bifurcation, see Fig. 13. The corresponding fixed point, TS, becomes stable again through a reverse sequence of period-doubling bifurcations before annihilating through the secondary saddle–node bifurcation. However, the basin of attraction becomes so thin that bursting begins to dominate the bi-stable dynamics of the model. Note that the bursting behavior becomes regular as the phase point passes through the upper section of the mapping

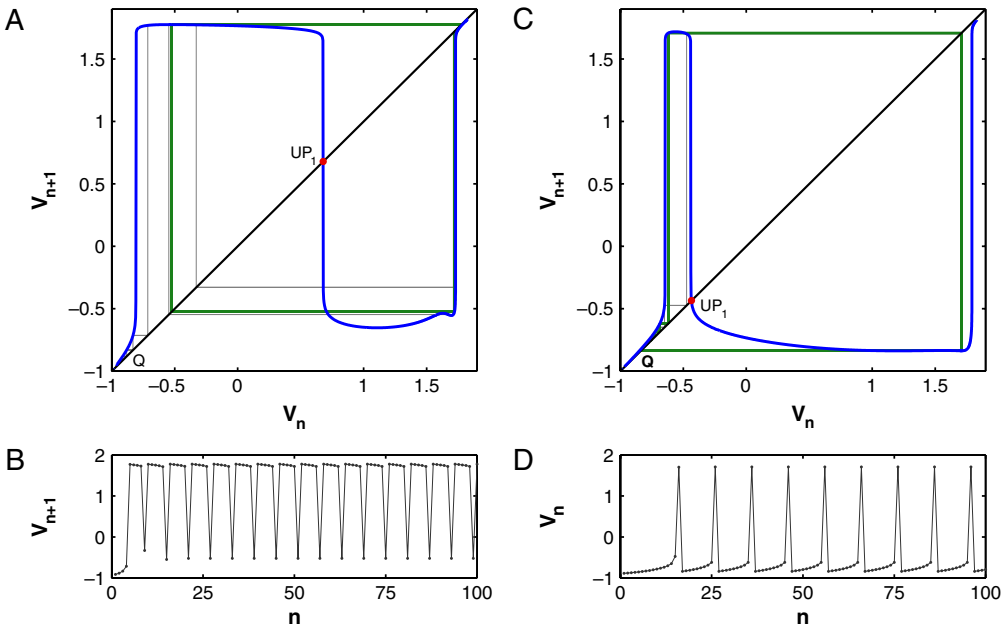

Fig. 14. (A) Periodic bursting with five spikes in the Poincaré interval mapping for the FitzHugh–Nagumo–Rinzel model at $c = -0.625$. The single unstable fixed point UP_1 separates the tonic spiking section of the mapping from the quiescent or subthreshold section (left). The number of iterates of the phase point adequately defines the ordinal type of bursting (B). Note the presence of a small hump around ($V_0 = 1.6, V_1 = -0.5$) which is an echo of the saddle–node bifurcation. (C) Poincaré return mapping at $c = -0.89$. The model is further hyperpolarized as the threshold, UP_1 moves further leftward so that the phase point makes more subthreshold oscillations, here nine, after a single spike per burst. (D) The voltage trace of 1–9 bursting: a single high amplitude spike is followed by nine subthreshold oscillations.

tangent to the bisectrix. The number of iterates that the orbit makes here determines the duration of the tonic spiking phase of bursting and is followed by a quiescence period initially comprised of a single iterate of the phase point to the right of the threshold UP_1. The evolution of bursting into MMO and on to subthreshold oscillations will be discussed in the next section.

4.2. From bursting to mixed-mode oscillations and quiescence

The disappearance of the tonic spiking orbit, TS, accords with the onset of regular bursting in the mapping and in the FitzHugh–Nagumo–Rinzel model (1). In the mapping a bursting orbit is comprised of iterates on the tonic spiking and quiescent sections separated by the unstable threshold fixed point, UP_1, of the mapping, Fig. 14. The shape of the graph undergoes a significant change reflecting the change in dynamics. The fixed points in the upper right section of the mapping disappears through a saddle–node bifurcation. One of the features of the saddle–node is the bifurcation memory such that the phase point continues to linger near a phantom of the disappeared saddle–node. The mapping near the bisectrix can generate a large number of iterates before the phase points diverges towards the quiescent phase. The larger the number of iterates near the bisectrix corresponds to a longer tonic spiking phase of bursting. Fig. 14 demonstrates how the durations of the phases change along with a change in the mapping shape: from a single quiescent iterate to the left of the threshold, UP_1, to a single tonic-spiking iterate corresponding to a bursting orbit with a single large spike in the model. Notice that, as the phase point is taken closer to the unstable section Q near $V = -1$, the quiescent phase of bursting becomes longer. The number of tonic spiking iterates decreases as the threshold fixed point moves to the left and the number of subthreshold oscillations increases. These "winding" numbers during the tonic spiking and quiescent phase define the ordinal type of bursting, for example 5–1 and example 1–9 shown respectively in Fig. 14 Insets (A), (B) and (C), (D).

The transition from bursting to quiescence in the model is not monotone because the regular dynamics may be sparked by episodes of chaos. Such subthreshold chaos in the corresponding mapping at $c = -0.9041$ is demonstrated in Fig. 15(A). This phenomena is labeled MMO because the small amplitude subthreshold oscillations are sporadically interrupted by larger spikes (Inset B). Use of the mapping makes the explanation of the phenomena in elliptic bursters particularly clear. In Fig. 15(A), after the mapping (or the model) fires a spike, the phase point is reinjected close to the threshold point, UP_1, from where it spirals away to make another cycle of bursting. Note that the number of iterates of the phase point around UP_1 may vary after each spiking episode. This gives rise to solutions that are called bi-asymptotic or homoclinic orbits to the unstable fixed point UP_1 (Inset C). The occupancy of such a homoclinic orbit to a repelling fixed point is the generic property of a one-dimensional non-invertible mapping [55], since the point of a homoclinic orbit might have two pre-images. Note that the number of forward iterates of a homoclinic point may be finite in a non-invertible mapping, because the phase point might not converge but merely jump onto the unstable fixed point after being reinjected. However, the number of backward iterates of the homoclinic point is infinite, because the repelling fixed point becomes an attractor for an inverse mapping in restriction to the local section of the unimodal mapping, see Fig. 15(C) and (D). The presence of a single homoclinic orbit leads to the abundance of other emergent homoclinics [56] via a homoclinic explosion [25].

A small decrease of the bifurcation parameter causes a rapid change in the shape of the mapping, as depicted in Fig. 15(A) and (C); the sharp peak near the threshold becomes lower such that the mapping can no longer generate large amplitude spikes. Instead of MMO dynamics, the mapping exhibits small-amplitude chaotic subthreshold oscillations, which are still caused by homoclinic orbits of the fixed point, UP_1. Loosely speaking, this means that the iterates of the mapping come close to the fixed point, that would be isolated in a lacuna otherwise. This fixed point corresponds to a single v-maximum of the saddle periodic orbit of the FitzHugh–Nagumo–Rinzel model. The orbit is located on the inner, cone-shaped section of the tonic-spiking manifold M_{lc}.

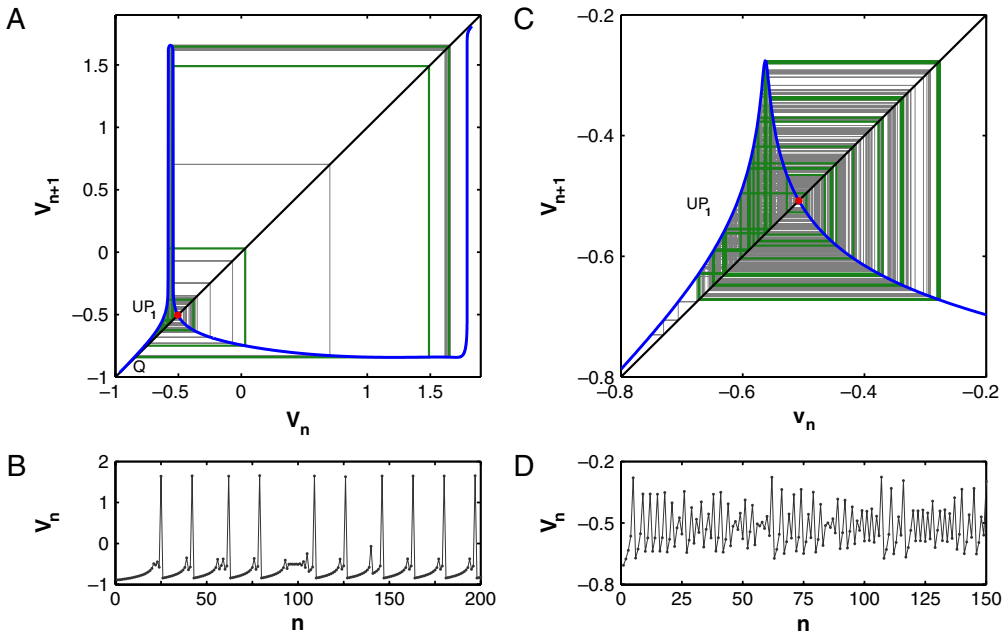

Fig. 15. (A) Chaotic MMO and bursting in the mapping at $c = -0.9041$ caused by the complex recurrent behavior around the unstable fixed point UP_1. (B) Subthreshold oscillations are disrupted sporadically by large and intermediate magnitude spikes thereby destroying the rhythmic bursting in the model. (C) Poincaré return mapping for the FitzHugh–Nagumo–Rinzel model shows no bursting but complex subthreshold oscillations at $c = -0.90476$. (D) After the peak in the mapping decreases in amplitude transforming into a cusp, thus making the occupancy of high amplitude spikes impossible. Here, chaos is caused by homoclinic orbits to the unstable fixed point UP_1.

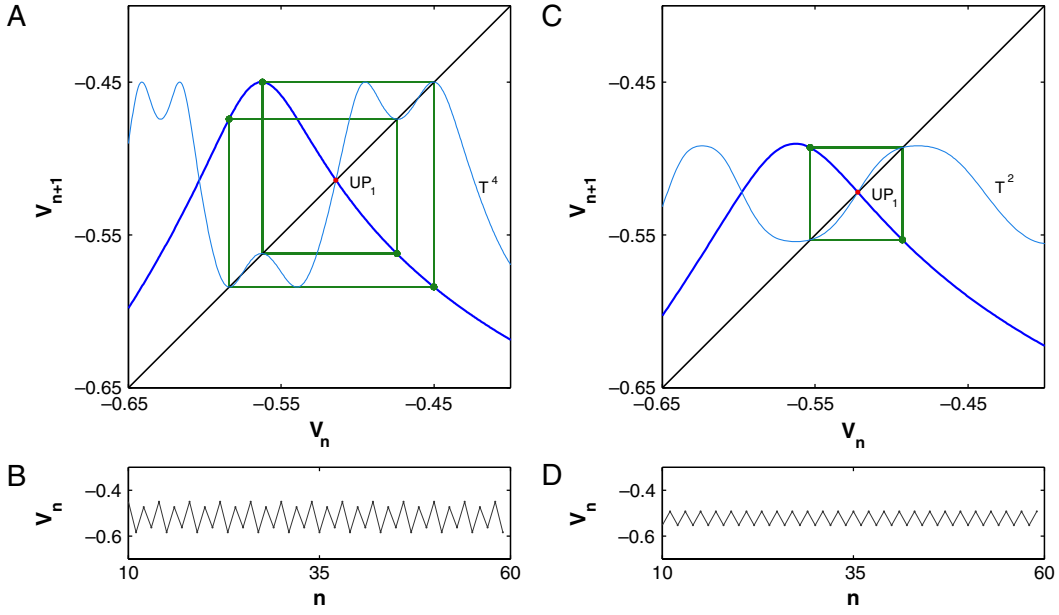

Fig. 16. (A) and (C) Stable period-4 and period-2 orbits (green) of the interval mapping at $c = -0.906$ and $c = -0.9075$. Shown in light-blue are the corresponding mappings T^4 and T^2 of degree four and two with four and two stable fixed points correspondingly. The traces of the orbits are shown in Insets (B) and (D). (For interpretation of the references to colour in this figure legend, the reader is referred to the web version of this article.)

As the parameter is decreased further, the unstable fixed point, UP_1, becomes stable through a reverse period-doubling cascade. The last two stages of the cascade are depicted in Fig. 16(A) and Fig. 17. Insets (A) and (C) of the former figure show stable period-4 and period-2 orbits, and their traces in Insets (B) and (D), as the parameter c is decreased from -0.906 to -0.9075. Here we demonstrate another ability of the interval mappings derived directly from the flow. In addition to the original mapping, T, in Fig. 16 we see two superimposed mappings, T^2 and T^4 (shown in light blue), of degree two and four respectively. The four points of the periodic orbit in Inset (A) correspond to the four fixed points of the fourth degree mapping T^4 at $c = -0.9075$, whereas the period-2 orbit in (C) correspond to two new fixed points of the mapping T^2 in (C) at $c = -0.9075$. We see clearly that both periodic orbits are indeed stable because of the slopes of the mappings at the fixed points on the bisectrix. Using the mappings of higher degrees we can evaluate the critical moments at which the period-2 and period-4 orbits are about to bifurcate. We point out that a period-doubling cascade, beginning with a limit cycle near the Hopf-initiated canard toward subthreshold chaos, has been recently reported in slow–fast systems [24,57].

Decreasing c further, the period-2 orbit collapses into the fixed point, UP_1, which becomes stable, Fig. 17 inset (A). The multiplier, first negative becomes positive but is still less than one in the

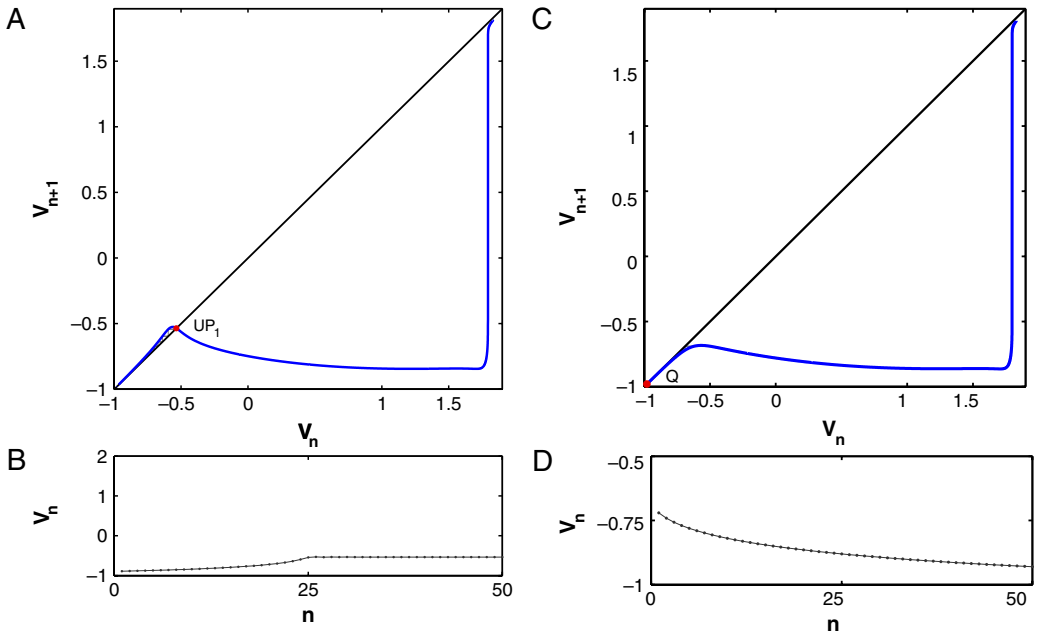

Fig. 17. (A) Full scale Poincaré return map at $c = -0.91$ has a single stable fixed point corresponding to a stable periodic orbit of the FitzHugh–Nagumo–Rinzel model exhibiting regular, periodic subthreshold oscillations. The oscillations are extinguished after the orbit collapses into the equilibrium state. Inset (C) shows the corresponding mapping with a stable fixed point near $V = -1$. (B) and (D) The voltage traces illustrating the transients converging to the periodic subthreshold orbit and the quiescent fixed point.

absolute value. When the fixed point lowers to the left bottom corner of the mapping near $V = -1$ the corresponding periodic orbit reaches the vertex of the tonic spiking manifold. In terms of the model, this means that the periodic orbit collapses into a saddle-focus through the subcritical Andronov–Hopf bifurcation. After that, the equilibrium state, located at the intersection of the manifold M_{eq} with the slow-nullcline (plane) in Fig. 3, becomes stable and the model goes into quiescence for parameter values smaller then $c = -0.97$, see Fig. 17(C). The stable equilibrium state corresponds to the fixed point, Q, which is the global attractor in the mapping.

5. Quantitative features of mappings: kneadings

In this section we discuss quantitative properties of the interval mappings for the dynamics of the model (1). In particular, we carry out the examination of complex dynamics with the use of calculus-based and calculus-free tools such as Lyapunov exponents and kneading invariants for the symbolic description of MMOs.

Chaos may be quantitatively measured by a Lyapunov exponent. The Lyapunov exponent is evaluated for one-dimensional mappings as follows:

$$\lambda = \lim_{N\to+\infty} \frac{1}{N} \sum_{i=1}^{N} \log |T'(v_i)|, \tag{3}$$

where $T'(v_i)$ is the slope (derivative) of the mapping at the current iterate v_i corresponding to the i-th step for $i = 0, \ldots, N$. Note that by construction the mapping graph is polygonal and to accurately evaluate the derivatives in (3) we used a cubic spline. The Lyapunov exponent, λ, yields a lower bound for the topological entropy $h(T)$ [58]; serving as a measure of chaos in a model. The Lyapunov exponent values $\lambda \simeq 0.24$ and $\lambda \simeq 0.58$, found for the interval mappings at $c = -0.9041$ and $c = -0.90476$ resp., show that chaos is developed more in the case of subthreshold oscillations than for MMOs.

The topological entropy may also be evaluated though a symbolic description of the dynamics of the mapping that requires no calculus-based tools. The curious reader is referred to [59,60] for the in-depth and practical overviews of the kneading invariants, while below we will merely touch on the relevant aspects of the theory. For unimodal mappings of an interval into itself with a single critical point v_c, like for the case $c = -0.90476$ (Fig. 18 inset B), we need only to follow the forward iterates of the critical point to generate the *unsigned kneading sequence* $\kappa(v_c) = \{\kappa_n(v_c)\}$ defined on $\{-1, +1\}$ by the following rule:

$$\kappa_n(v_q) = \begin{cases} +1, & \text{if } T^n(v_c) < v_c \\ -1, & \text{if } T^n(v_c) > v_c, \end{cases} \tag{4}$$

where $T^n(v_c)$ is the n-th iterate of the critical point v_c.

The kneading invariant of the unimodal mapping is a series of the *signed kneadings* $\{\tilde{\kappa}_n\}$ of the critical point, which are defined through the unsigned kneadings, κ_i, as follows:

$$\tilde{\kappa}_n = \prod_{i=1}^{n} \kappa_i, \tag{5}$$

or, recursively:

$$\tilde{\kappa}_n = \kappa_n \tilde{\kappa}_{n-1}, \quad i = 2, 3, \ldots. \tag{6}$$

Next we construct a formal power series;

$$P(t) = \sum_{i=0}^{\infty} \tilde{\kappa}_i t^i. \tag{7}$$

The smallest zero, t^* (if any), of the series within an interval $t \in (0, 1)$ defines the topological entropy, $h(T) = \ln(1/t^*)$. The sequence of the signed kneadings, truncated to the first ten terms, $\{-+++-+++-+\}$ for the mapping in Fig. 18 inset B, generates the polynomial $P_{10}(t) = -1+t+t^2+t^3-t^4+t^5+t^6+t^7-t^8+t^9$. The single zero of $P_{10}(t)$ at $t^* \approx 0.544779$ yields a close estimate for the topological entropy $h(T) \approx 0.6073745$, see Fig. 18(A). The advantage of an approach based on the kneading invariant to quantify chaos is that evaluation of the topological entropy does not involve numerical calculus for such equationless interval mappings, but relies on the mixing properties of the dynamics

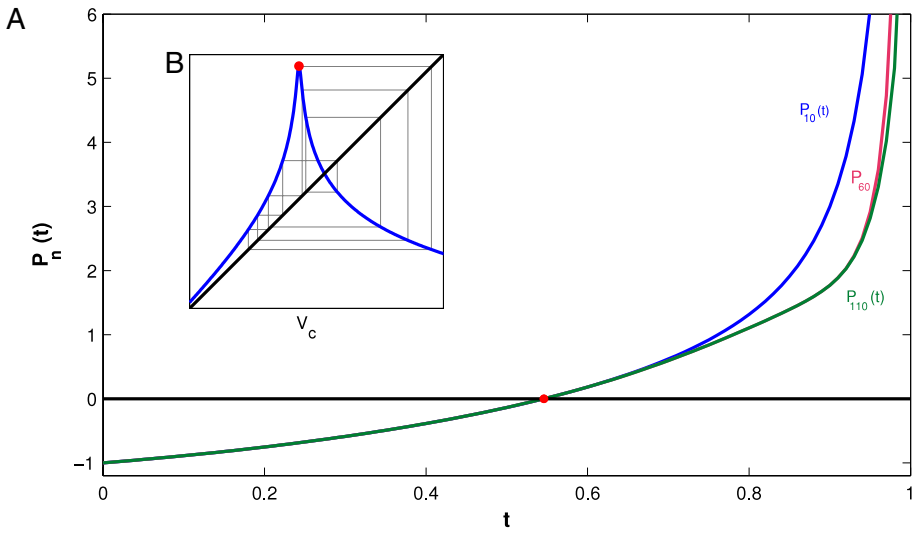

Fig. 18. (A) Graphs of the three polynomials, $P_{10}(t)$, $P_{60}(t)$ and $P_{110}(t)$ defined on the unit interval, and generated through the series of signed kneadings at $c = -0.90476$. Inset (B) shows the corresponding interval mapping. The iterates of the critical point, v_c, determine the symbolic dynamics for the unsigned kneading symbols: -1 if the phase point lands on the decreasing section of the mapping graph to the right of the critical point, and $+1$ if it lands on the increasing section of the mapping, which is to the left of the critical point.

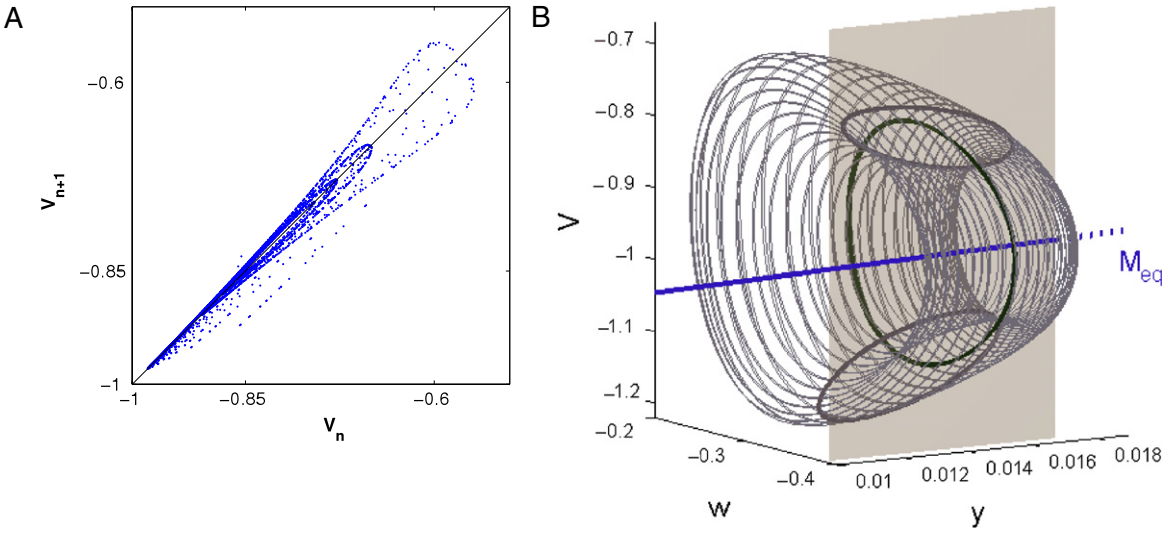

Fig. 19. (A) Pointwise mapping for $c = -0.945$ obtained from voltage traces using random initial conditions clearly illustrating a torus formation in the subthreshold voltage oscillations. (B) A repelling torus leaving two circles on the cross-section bounds the attraction basin of the subthreshold stable periodic orbit emerging through a supercritical Andronov–Hopf bifurcation.

instead. Moreover, it requires a relatively few forward iterates of the critical point to compute the entropy relatively accurately, as the polynomial graphs in Fig. 18 suggests. Besides yielding the quantitative information such as the topological entropy, the symbolic description based on the kneading invariants provides qualitative information for identifying the corresponding Farey sequences describing the MMOs in terms of the numbers of subthreshold and tonic spiking oscillations.

6. Discussion

We present a case study for an in-depth examination of the bifurcations that take place at activity transitions between tonic spiking, bursting and mixed mode oscillations in the FitzHugh–Nagumo–Rinzel model. The analysis is accomplished through the reduction to a single-parameter family of equationless Poincaré return mappings for an interval of the "voltage" variable. We stress that these mappings are *models* themselves for evaluating the complex dynamics of the full three-dimensional model. Nevertheless the dynamics of the single accumulative variable, v, reflects the cooperative dynamics of other variables in the model. The reduction is feasible since the model is a slow–fast system and, hence, possesses a two-dimensional, slow-motion tonic-spiking manifold around which the oscillatory solutions of the models linger. While a reduction to a slow variable through the averaging equation such as (2) might seem more mathematically sound [31,30,25,33,34], for the sake of applicability of our results we show the computational technique for the mappings. We have specifically concentrate on the dynamics of the voltage [18,47], as it is typically the only measurable, and thus comparable, variable in experimental studies in neuroscience and physical chemistry.

The algorithm for interval mapping construction has two stages. First, one needs to identify the tonic spiking manifold in the phase space of the slow–fast neuron model in question. This is accomplished by either using the geometric dissection method, or the parameter continuation technique. The more accurately

and completely the first stage is performed the more natural and smooth these numerically derived mappings will be. The second stage is to build the mappings for a range of parameter values. The analysis of such mappings lets one identify not only attractors, but more importantly, the unstable sets including fixed, periodic and homoclinic orbits, which are known to be the globally organizing centers governing the dynamics of any model. In addition, having computationally smooth mappings allows one to create symbolic descriptions for dynamics, compute kneading invariants, evaluate Schwarzian derivatives, etc, as well as estimating other quantities measuring the degree of complexity for the trajectory behavior like Lyapunov exponents and topological entropy.

Our computational method allows us to thoroughly describe the bifurcations that the model (1) undergoes while transitioning between states: from tonic spiking to bursting and then to quiescence. Taken individually, each mapping offers only a glimpse into the system behavior. However, with an entire family of mappings we obtain a deep insight into the evolution of the model's dynamics through the interplay and bifurcations of the fixed points and periodic orbits of the mappings. This allows for not only the description of bifurcations *post factum*, but also to predict the changes in the dynamics of the model under consideration before they actually occur. The predicting ability of our technique helps to classify all bifurcations in the models of elliptically bursting neurons. We accomplished this through a comparison of the family of mappings derived for the FitzHugh–Nagumo–Rinzel model with the family of mappings of other models without explicitly finding the bifurcations occurring in other models.

Finally, we mention the cons of the approach. First there is a price to pay for the scrutiny as such simulations are time expensive. Another minor drawback of the approach is a small detuning offset in parameter values at which the model and the mapping have nearly the same dynamics, matching orbits, or undergo the same bifurcations. This is caused by the fact that a one-dimensional mapping for a single voltage variable does not fully encompass the dynamics of other, major and minor, variables of the corresponding model. In general, most features of a dissipative model with a negative divergence of the vector field, that results in a strong contraction of the phase volumes, are adequately modeled by a 1D Poincaré mapping. However, this is not true when such a contraction is no longer in place. For example, when the divergence becomes sign-alternating. There are two such places near the manifold $M_{\rm lc}$ in the model (1): one is near the fold, while the second is close to the cone-shaped tip where the model has an equilibrium state of the saddle-focus type with a pair of complex conjugate eigenvalues with small positive real part and a real negative eigenvalue due to the Andronov–Hopf bifurcation and the smallness of ε.

Under the above conditions a (small) torus can possibly occur locally in the phase space. A small canard torus at $c = -0.945$ is shown in Fig. 19(B). The torus is unstable: it bounds a basin of attraction of stable periodic orbit that emerged through the supercritical Andronov–Hopf bifurcation. As c increases, the torus collapses into the periodic orbit (see the bifurcation diagram in Fig. 4) and makes the orbit unstable. The unstable orbit then initiates the period-doubling cascade for the subthreshold oscillations depicted in Fig. 5(B) and captured in the mappings in Figs. 15 and 16. The stability of the torus near the single equilibrium state of the model, a saddle-focus, can be evaluated through the examination of the Lyapunov exponents, as their sum yields the divergence. Hence, making the middle equation of the model (1) faster by setting $\delta = 0.5$ changes the type of the torus bifurcation from sub- to supercritical. The stages of the torus's formation and vanishing are depicted in Fig. 21. The stable torus emerges from a periodic orbit with complex Floquet multipliers (Fig. 21(A) and (B)). Then it comes close to the fold of the manifold $M_{\rm lc}$ (Fig. 20),

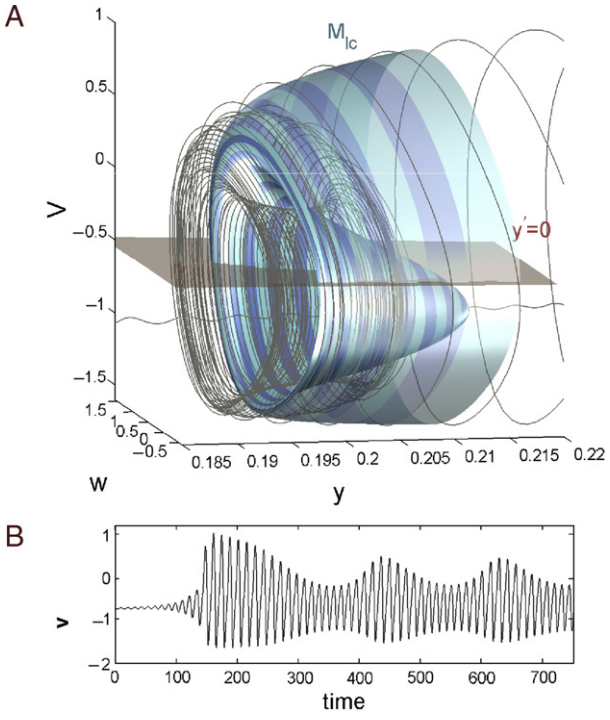

Fig. 20. (A) a 2D torus near the fold of the tonic spiking manifold $M_{\rm lc}$ at $\delta = 0.5$ and $c = -0.38$. (B) Voltage trace revealing slow ($\sim \mu$) characteristic modulation of oscillations.

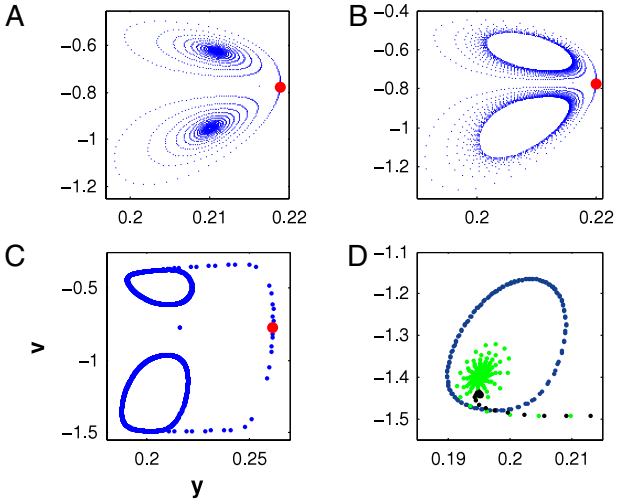

Fig. 21. 2D cross-section $w = -0.09$ revealing the stages of the torus's formation and vanishing in the model at $\delta = 0.5$: (A) stable periodic orbit (two spiraling-onto points) at $c = -0.55$ loses stability to a 2D torus (B) (two circles) at $c = -0.5478$ that, having approached the fold on the tonic spiking manifold $M_{\rm lc}$ at $c = -0.53$ (C) and (D) at $c = -0.45$ (dark blue), shrinks back to the tonic spiking periodic orbit at $c = 0.363$ (green) and 0.3 (black). Shown in red is the saddle-focus equilibrium state of the model. (For interpretation of the references to colour in this figure legend, the reader is referred to the web version of this article.)

where it shrinks back to the periodic orbit that corresponds to the tonic spiking activity in the model. It should be noted that, since for smaller values of δ the divergence of the vector field of this 3D model is negative near the fold, the stability loss of the nearby periodic orbit initiates a period-doubling cascade instead of the torus bifurcation, see also [19].

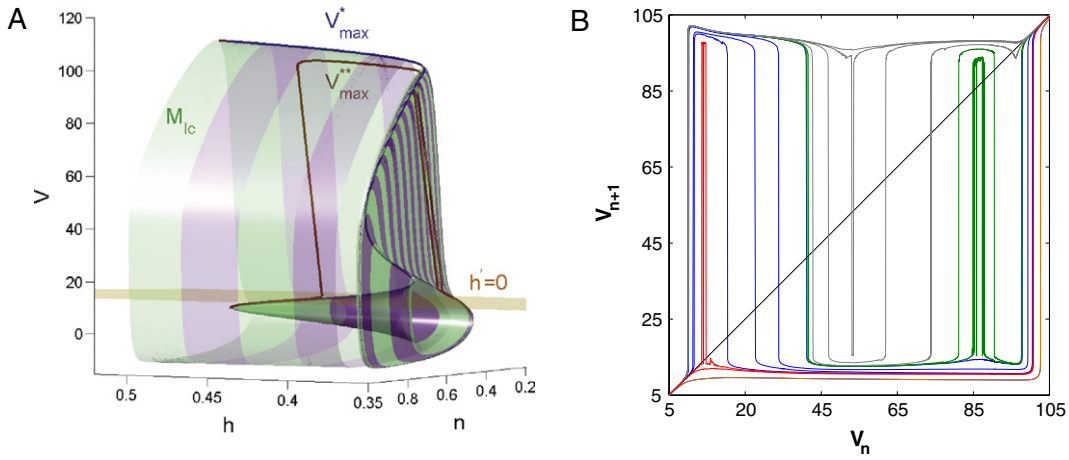

Fig. 22. (A) Tonic spiking manifold M_{lc} on the (n, h, V)-projection of the phase space for the Hodgkin–Huxley model. Plane $h' = 0$ is the slow nullcline. The mappings are defined on the space curve V^{*}_{max} made of local maxima of the periodic orbits spanning M_{lc}. Near the unstable, "canard" section of M_{lc} the points initiated on V^{*}_{max} return to the curve V^{**}_{max} instead. (B) Family of Poincaré return mappings for the bursting Hodgkin–Huxley model as the bifurcation parameter c is varied between -0.19 and -0.05.

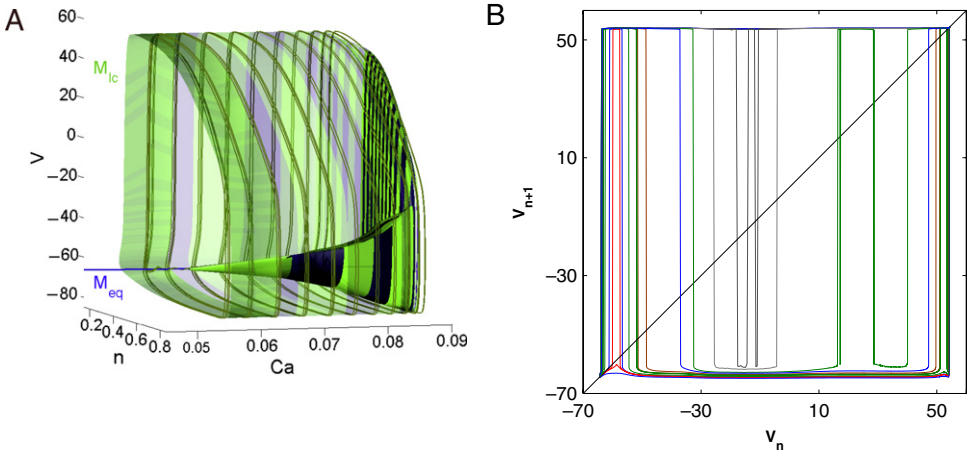

Fig. 23. Tonic spiking M_{lc} and quiescent M_{eq} manifolds in the (n, Ca, V)-projection of the phase space of the Rubin–Terman model. Shown in light color are bursting oscillations. (B) The GPe mapping family displays the typical shape for the Poincaré return mappings of the maximal voltage values in all three models of the elliptic buster.

It is evident that no 1D return mapping of the interval is intended to detect a torus in the phase plane, whereas the pointwise mappings generated by a forward time series of the voltage can identify the torus formation in the phase space, Fig. 19. Note that the torus has a canard-like nature, that is the torus exists within a narrow parameter window. A torus formation in a 3D model with two slow variables near the fold was reported also in [61]. Another parallel of the FitzHugh–Nagumo–Rinzel model with electrochemical systems, including the Belousov–Zhabotinky reaction, is that the latter also demonstrates a quasiperiodic regime [62]. The emergence of the torus near the fold of the tonic spiking manifold first described in [44,19] has turned out to be a generic phenomenon observed recently in several plausible models [63,64], including a model for the Purkinje cells [54,65], and in a 12D hair cell model [66].

Our future plan is to further develop the tools of the Poincaré return mappings for voltage intervals to study complex, slow–fast dynamics and activity transitions in some representative high-order models of square-wave busting interneurons identified in several central pattern generators.

Acknowledgments

We would like to thank Paul Channell, Alex Neiman, Bryce Chung and Summer (Xia) Hu for useful comments. This work was supported in part by the GSU Brains and Behavior program, RFFI grant No. 050100558, "Grant opportunities for Russian scientists living abroad" project #14.740.11.0919, and NSF grant DSM 1009591.

Appendix. Poincaré mappings for the bursting Hodgkin–Huxley model and the GPe Rubin–Terman model

The interval mappings capture the key features common for the models belonging to the same elliptic class. Here we present for comparison the families of the return mappings and the slow-motion tonic spiking manifolds for two other, exemplary models of elliptic bursters: the four-dimensional "bursting" adaptation of the classical Hodgkin–Huxley model [36] and the five-dimensional Rubin–Terman model for the external segment of the Globus Pallidus [67]. The similarities of the manifolds are evident as are the similarities of the mappings for all three models, see Figs. 22 and 23. Note the "instability" of vertical sections in the mappings; this instability is due to exponentially fast transitions between the slow-motion manifolds, tonic spiking M_{lc} and quiescent M_{eq}, compared to the change in rate of the slowest variable in each given model. Also worth mentioning is the instability of the middle, unstable section of M_{lc}, comprised of the saddle or canard-like periodic orbits. As the result of this instability, the mapping may take the space curve V^{*}_{max} not exactly into itself, as meant by

construction, but to a curve close to $V^{**}_{\max}$, depicted in Fig. 22 for the bursting Hodgkin–Huxley model. For sake of compatibility, the equations of the bursting version of the models used are given "as is" so the reader can cut-and-paste directly from this pdf document. The first is a bursting Hodgkin–Huxley model [36]:

$$\begin{aligned}
\mathtt{V}' &= 2 + 36 * \mathtt{pow}(\mathtt{n}, 4) * (-12 - \mathtt{V}) + 60 * \mathtt{pow}(\mathtt{m}, 3) * \mathtt{h} \\
&\quad * (115 - \mathtt{V}) + 0.3 * (10.613 - \mathtt{V});\\
\mathtt{n}' &= 0.005 * (-\mathtt{V} + 10)/(\exp(-0.1 * \mathtt{V} + 1) - 1) \\
&\quad * (1 - \mathtt{n}) - 0.125 * \exp(-\mathtt{V}/11) * \mathtt{n};\\
\mathtt{m}' &= 0.1 * (-\mathtt{V} + 25)/(\exp(-0.1 * \mathtt{V} + 2.5) - 1) * (1 - \mathtt{m}) \\
&\quad - 4 * \exp(-\mathtt{V}/18) * \mathtt{m};\\
\mathtt{h}' &= 0.002 * (0.2 * \exp(-\mathtt{V}/20) * (1 - \mathtt{h}) \\
&\quad - 1/(\exp(-0.1 * \mathtt{V} + 3) + 1) * \mathtt{h} + \mathtt{c}).
\end{aligned}$$

In the model, $c \in [-0.19, -0.05]$ is the sweeping parameter used to scan the slow motion manifold M_{lc}, as well as generate the corresponding mapping family sampled in Fig. 22. Note that c only moves the slow nullcline given $h' = 0$ in the phase space of the model.

The third model of the elliptic burster considered in this study was proposed and studied in [67]. The model is meant to describe the voltage dynamics in the external segment of the Globus Pallidus in connection with complex oscillatory activity observed in neurons of the basal ganglia. The equations for the model are read as follows:

$$\begin{aligned}
\mathtt{V}' &= -0.1 * (\mathtt{V} + 55) - 30 * \mathtt{pow}(\mathtt{n}, 4) * (\mathtt{V} + 80) - 120 \\
&\quad * \mathtt{pow}(1/(1 + \exp(-(\mathtt{V} + 37)/10)), 3) * \mathtt{h} * (\mathtt{V} - 55) \\
&\quad - 0.5/(1 + \exp(-(\mathtt{V} + 57)/2)) * \mathtt{pow}(1/(1 + \exp(\\
&\quad - (\mathtt{V} + 57)/2)), 2) * \mathtt{r} * (\mathtt{V} - 120) - 0.15 * \mathtt{pow}(1/(1 \\
&\quad + \exp(-(\mathtt{V} + 35)/2)), 2) * (\mathtt{V} - 120) - 30 * (\mathtt{V} + 80) \\
&\quad * (\mathtt{Ca}/(\mathtt{Ca} + 30));\\
\mathtt{n}' &= 0.05 * ((1/(1 + \exp(-(\mathtt{V} + 50)/14)) - \mathtt{n})/(0.05 \\
&\quad + 0.27/(1 + \exp((\mathtt{V} + 40)/12))));\\
\mathtt{h}' &= 0.05 * ((1/(1 + \exp((\mathtt{V} + 58)/12)) - \mathtt{h})/(0.05 \\
&\quad + 0.27/(1 + \exp((\mathtt{V} + 40)/12))));\\
\mathtt{r}' &= (1/(1 + \exp((\mathtt{V} + 70)/2)) - \mathtt{r})/30;\\
\mathtt{Ca}' &= \epsilon * (-0.15 * \mathtt{pow}(1/(1 + \exp(-(\mathtt{V} + 35)/2)), 2) \\
&\quad * (\mathtt{V} - 120) - 0.5 * \mathtt{pow}(1/(1 + \exp(-(\mathtt{V} + 57)/2)), 3) \\
&\quad * \mathtt{r} * (\mathtt{V} - 120) - 20 * \mathtt{Ca} + \mathtt{c});
\end{aligned}$$

with $\epsilon = 0.0001$; here c is a sweeping parameter in the slow equation used to detect the tonic spiking, M_{lc}, and quiescent manifolds in the phase space of the model, see Fig. 23.

The reader is referred to the original work that discusses the subjects of the model, and examines in detail the dynamics and bifurcations in it. The Rubin–Terman model is employed here to test the algorithm for mapping derivations and verify that intrinsically the mappings for the model are shaped uniformly similar across a diverse set of the class of elliptic bursters. The tonic spiking and quiescent manifolds, as well as the family of Poincaré return mappings for an interval of the maximal voltage values, are shown in Fig. 23. The tonic spiking manifold has the characteristic cone-like shape indicating a subthreshold Andronov–Hopf bifurcation, and the fold corresponding to a saddle–node bifurcation. The family of mappings for an interval of the voltage, "accumulating" the dynamics of all other currents, including calcium, reveals the close similarity to the return mappings for all three elliptic busters discussed in this paper.

References

[1] N. Kopell, Toward a theory of modelling central pattern generators, in: A.H. Cohen, S. Rossingol, S. Grillner (Eds.), Neural Control of Rhythmic Movements in Vertebrates, Wiley, New York, 1988.

[2] E. Marder, R.L. Calabrese, Principles of rhythmic motor pattern generation, Physiol. Rev. 76 (3) (1996) 687–717.

[3] J. Rinzel, A formal classification of bursting mechanisms in excitable systems, in: Proc. International Congress of Mathematics, AMS, 1987, pp. 1578–1593.

[4] J. Rinzel, Y.S. Lee, Dissection of a model for neuronal parabolic bursting, J. Math. Biol. 25 (6) (1987) 653–675.

[5] R. Bertram, M.J. Butte, T. Kiemel, A. Sherman, Topological and phenomenological classification of bursting oscillations, Bull. Math. Biol. 57 (3) (1995) 413–439.

[6] J. Guckenheimer, Towards a global theory of singularly perturbed systems, Progr. Nonlinear Differential Equations Appl. 19 (1996) 214–225.

[7] E.M. Izhikevich, Dynamical Systems in Neuroscience. The Geometry of Excitability and Bursting, MIT Press, Cambridge, Mass, 2007.

[8] J. Rinzel, X.J. Wang, Oscillatory and bursting properties of neurons, in: M. Arbib (Ed.), The Handbook of Brain Theory and Neural Networks, MIT Press, 1995, pp. 686–691.

[9] V.I. Arnold, V.S. Afraimovich, Yu.S. Ilyashenko, L.P. Shilnikov, Bifurcation theory, in: Dynamical Systems. Encyclopaedia of Mathematical Sciences, vol. V, Springer, 1994.

[10] F. Fenichel, Geometric singular perturbation theory for ordinary differential equations, J. Differential Equations 31 (1979) 53–98.

[11] E.F. Mischenko, N.K. Rozov, Differential Equations with Small Parameters and Relaxation Oscillations, Plenum Press, 1980.

[12] E.F. Mischenko, Yu.S. Kolesov, A.Yu. Kolesov, N.Kh. Rozov, Asymptotic Methods in Singularly Perturbed Systems, in: Monographs in Contemporary Mathematics, Consultants Bureau, New York, 1994.

[13] L.S. Pontryagin, L.V. Rodygin, Periodic solution of a system of ordinary differential equations with a small parameter in the terms containing derivatives, Sov. Math. Dokl. 1 (1960) 611.

[14] A.N. Tikhonov, On the dependence of solutions of differential equations from a small parameter, Mat. Sb. 22 (64) (1948) 193–204.

[15] A.I. Neishtadt, On delayed stability loss under dynamical bifurcations I, Differ. Equ. 23 (1988) 1385–1390.

[16] A.I. Neishtadt, On delayed stability loss under dynamical bifurcations II, Differ. Equ. 24 (1989) 171–176.

[17] V.N. Belykh, I.V. Belykh, M. Colding-Jorgensen, E. Mosekilde, Homoclinic bifurcations leading to bursting oscillations in cell models, Eur. Phys. J. E 3 (3) (2000) 205–219.

[18] P. Channell, G. Cymbalyuk, A. Shilnikov, Origin of bursting through homoclinic spike adding in a neuron model, Phys. Rev. Lett. 98 (13) (2007) 134101.

[19] G. Cymbalyuk, A.L. Shilnikov, Coexistence of tonic spiking oscillations in a leech neuron model, J. Comput. Neurosci. 18 (3) (2005) 255–263.

[20] U. Feudel, A. Neiman, X. Pei, W. Wojtenek, B. Braun, M. Huber, F. Moss, Homoclinic bifurcation in a hodgkin-huxley model of thermally sensitive neurons, Chaos 10 (1) (2000) 231–239.

[21] A.V. Holden, Y.S. Fan, From simple to simple bursting oscillatory behaviour via intermittent chaos in the Rose–Hindmarsh model for neuronal activity, Chaos Solitons Fractals 2 (1992) 349–369.

[22] A.L. Shilnikov, R.L. Calabrese, G. Cymbalyuk, Mechanism of bistability: tonic spiking and bursting in a neuron model, Phys. Rev. E: Stat. Nonlinear Soft Matter Phys. 71 (2005) 056214. 5 Pt 2.

[23] D. Terman, The transition from bursting to continuous spiking in excitable membrane models, J. Nonlinear Sci. 2 (2) (1992) 135–182.

[24] M.A. Zaks, X. Sailer, L. Schimansky-Geier, A.B. Neiman, Noise induced complexity: from subthreshold oscillations to spiking in coupled excitable systems, Chaos 15 (2) (2005) 26117.

[25] L.P. Shilnikov, A.L. Shilnikov, D. Turaev, L.O. Chua, Methods of Qualitative Theory in Nonlinear Dynamics, vols. 1 and 2, World Scientific, Singapore, 1998, 2001.

[26] F.N. Albahadily, J. Ringland, M. Schell, Mixed-mode oscillations in an electrochemical system. I. A farey sequence which does not occur on a torus, J. Chem. Phys. 90 (2) (1989) 813–822.

[27] P. Gaspard, X.J. Wang, Homoclinic orbits and mixed-mode oscillations in far-from-equilibrium, J. Stat. Phys. 48 (1–2) (1987) 151–199.

[28] M. Koper, Bifurcations of mixed-mode oscillations in a three-variable autonomous van der pol-duffing model with a cross-shaped phase diagram, Phys. D 80 (1–2) (1995) 72–94.

[29] J.L. Hudson, D. Marinko, An experimental study of multiple peak periodic and nonperiodic oscillations in the Belousov–Zhabotinskii reaction, J. Chem. Phys. 71 (4) (1979) 1601–1606.

[30] R.E. Griffiths, M.C. Pernarowski, Return map characterizations for a model of bursting with two slow variables, SIAM J. Appl. Math. 66 (6) (2006) 1917–1948.

[31] G.M. Medvedev, Reduction of a model of an excitable cell to a one-dimensional map, Physica D 202 (1–2) (2005) 87–106.

[32] G.M. Medvedev, Transition to bursting via deterministic chaos, Phys. Rev. Lett. 97 (2006) 048102.

[33] A.L. Shilnikov, M.L. Kolomiets, Methods of the qualitative theory for the Hindmarsh–Rose model: a case study. A tutorial, Int. J. Bifurcation Chaos 18 (7) (2008) 1–32.

[34] A.L. Shilnikov, L.P. Shilnikov, D.V. Turaev, Blue sky catastrophe in singularly perturbed systems, Mosc. Math. J. 5 (1) (2005) 205–211.

[35] V.N. Belykh, E.V. Pankratova, Chaotic synchronization in ensembles of coupled neurons modeled by the Fitzhhugh–Rinzel system, Radiophys. and Quantum Electronics 49 (11) (2006) 910–921.

[36] E.M. Izhikevich, Synchronization of elliptic bursters, SIAM Rev. 43 (2) (2001) 315–344.

[37] G. Medvedev, J. Cisternas, Multimodal regimes in a compartmental model of the dopamine neuron, Physica D 194 (2004) 333–356.

[38] S. Popovych, A. Gail, J. Schropp, Complex dynamics of a single neuron model, Phys. Rev. E Statist. Nonlinear Soft Matter Phys. 74 (4 Pt 1) (2006) 041914.
[39] J. Su, J. Rubin, D. Terman, Effects of noise on elliptic bursters, Nonlinearity 17 (2004) 133–157.
[40] A. Arneodo, F. Argoul, J. Elezgaray, P. Richetti, Homoclinic chaos in chemical system, Physica D 62 (1993) 134–169.
[41] J. Doi, S. Kumagai, Generation of very slow neuronal rhythms and chaos near the hopf bifurcation in single neuron models, J. Comput. Neurosci. 19 (3) (2005) 325–356.
[42] M. Krupa, N. Popovich, N.J. Kopell, Mixed-mode oscillations in three time-scale systems: a prototypical example, SIAM J. Appl. Dyn. Syst. 7 (2) (2008) 361–420.
[43] J. Rubin, M. Wechselberger, The selection of mixed-mode oscillations in a Hodgkin–Huxley model with multiple timescales, Chaos 18 (2008) 015105–015117.
[44] A.L. Shilnikov, N.F. Rulkov, Origin of chaos in a two-dimensional map modelling spiking-bursting neural activity, Internat. J. Bifur. Chaos 13 (11) (2003) 3325–3340.
[45] A.L. Shilnikov, N.F. Rulkov, Subthreshold oscillations in a map-based neuron model, Phys. Lett. A 328 (2–3) (2004) 177–184.
[46] P. Channell, G. Cymbalyuk, A.L. Shilnikov, Applications of the poincare mapping technique to analysis of neuronal dynamics, Neurocomputing 70 (2007) 10–12.
[47] P. Channell, I. Fuwape, A.B. Neiman, A.L. Shilnikov, Variability of bursting patterns in a neuron model in the presence of noise, J. Comput. Neurosci. 27 (3) (2009) 527–542.
[48] M. Koper, P. Gaspard, Mixed-mode and chaotic oscillations in a simple model of electrochemical osillator, J. Phys. Chem. 95 (1991) 4945–4947.
[49] M. Koper, P. Gaspard, Mixed-mode oscillations and incomplete homoclinic scenarios to a saddle-focus in the indium/thiocyanate electrochemical oscillators, J. Chem. Phys. 97 (11) (1992) 8250–8260.
[50] T.R. Chay, Chaos in a three-variable model of an excitable cell, Physica D 16 (2) (1985) 233–242.
[51] M. Koper, P. Gaspard, J. Sluyters, Mixed-mode oscillations and incomplete homoclinic scenarios to a saddle-focus in the indium/thiocyanate electrochemical oscillator, J. Chem. Phys. 97 (11) (1992) 8250–8260.
[52] A.L. Shilnikov, On bifurcations of the Lorenz attractor in the Shimizu–Morioka model, Physica D 62 (1–4) (1993) 338–346.
[53] Yu. Kuznetsov, ftp://ftp.cwi.nl/pub/CONTENT.
[54] M.A. Kramer, R.D. Traub, N.J. Kopell, New dynamics in cerebellar purkinje cells: torus canards, Phys. Rev. Lett. 101 (6) (2008) 068103.
[55] C. Mira, Chaotic Dynamics from the One-Dimensional Endomorphism to the Two-Dimensional Diffeomorphism, World Scientific, Singapore, 1987.
[56] N.K. Gavrilov, L.P. Shilnikov, On three-dimensional dynamical systems close to systems with a structurally unstable homoclinic curve, Math. USSR Sb. 17 (3) (1972) 467–485.
[57] M. Zaks, On chaotic subthreshold oscillations in a simple neuronal model, Math. Model. Nat. Phenom. 6 (1) (2011) 1–14.
[58] A.B. Katok, Lyapunov exponents, entropy and periodic orbits for diffeomorphisms, Publ. Math. Inst. Hautes Études Sci. 51 (1980) 137–173.
[59] P. Glendinning, T. Hall, Zeros of the kneading invariant and topological entropy for Lorenz maps, Nonlinearity 9 (1996) 999–1014.
[60] M.-C. Li, M. Malkin, Smooth symmetric and Lorenz models for unimodal maps, Internat. J. Bifur. Chaos 13 (11) (2003) 3353–3371.
[61] J. Guckenheimer, Singular hopf bifurcation in systems with two slow variables, SIAM J. Appl. Dyn. Syst. 7 (4) (2008) 1355–1377.
[62] F. Argoul, J.C. Roux, Quasiperiodicity in chemistry: an experimental path in the neighborhood of a codimension-two bifurcation, Phys. Lett. A 108 (8) (1985) 426–430.
[63] A. Kuznetsov, S. Kuznetsov, N.V. Stankevich, A simple autonomous quasiperiodic self-oscillator, Commun. Nonlinear Sci. Numer. Simul. 15 (2010) 1676–1681.
[64] A. Shilnikov, L. Shilnikov, Torus conditions in slow–fast models (2010) (in preparation).
[65] N. Benes, A. Barry, T. Kaper, M. Kramer, J. Burke, An elementary model of torus canards. J. Chaos (2010) (submitted for publication).
[66] A. Neiman, A. Shilnikov, Spontaneous voltage oscillations enhance sensitivity of saccular hair cells. J Neurophysiol. (2011) (submitted for publication).
[67] D. Terman, J.E. Rubin, A.C. Yew, C.J. Wilson, Activity patterns in a model for the subthalamopallidal network of the basal ganglia, J. Neurosci. 22 (7) (2002) 2963–2976.